Technische Universität München
TUM School of Medicine and Health

TITI

Quantitative magnetic resonance imaging of human supraclavicular fat in association to cold-induced thermogenesis for the detection of brown adipose tissue

Cora Held

Vollständiger Abdruck der von der TUM School of Medicine and Health der Technischen Universität

München zur Erlangung einer

Doktorin der Medizin (Dr. med.)

genehmigten Dissertation.

Vorsitz: Prof. Dr. Gabriele Multhoff

Prüfende der Dissertation:

1.   Prof. Dimitrios Karampinos, Ph.D.
2.   Prof. Dr. Franz Schilling

Die Dissertation wurde am 11.10.2023 bei der Technischen Universität München eingereicht und

durch die TUM School of Medicine and Health am 10.04.2024 angenommen.

1 <u>Abstract</u>

Human adipose tissue can be mainly divided in to two different forms: white adipose tissue (WAT) and brown adipose tissue (BAT). The main function of WAT is energy storage, while BAT produces heat to maintain body temperature. BAT is activated under cold exposure and increases resting energy expenditure, a process also called cold-induced thermogenesis (CIT). This uptake in calory combustion renders BAT a promising treatment target for obesity and metabolic dysfunction. Dedicated magnetic resonance imaging (MRI) techniques, measuring the fat fraction of a tissue, are promising non-invasive tools to detect or even quantify BAT. Especially the proton density fat fraction (PDFF) of the supraclavicular fossa is known to decrease with the presence of BAT. It was the purpose of this research to investigate this inverse relationship of supraclavicular PDFF ($PDFF_{SC}$) and CIT, to establish $PDFF_{SC}$ as a possible surrogate marker for CIT.

This explorative study followed a two-phased design. In phase one CIT values were conducted from healthy volunteers recruited via bulletin and in a second phase MRI measurements were performed on a sub cohort. CIT was assessed under cold exposure in strictly controlled conditions via indirect calorimetry. MRI measurements were performed under thermoneutral conditions and semi-automatic data processing insured data quality. For the statistical analysis of the very heterogenous cohort (39 participants) non-parametric testing (Wilcoxon) and spearman's rank correlation coefficient were used.

In contrast to the hypothesis no significant relation between $PDFF_{SC}$ and CIT was found. A thorough exploration of the data revealed adiposity as a strong confounding factor. Therefore, gluteal PDFF ($PDFF_{GLU}$) measurements, depicting a typical WAT depot, were used to correct for confounding adiposity and a new marker the delta PDFF ($PDFF_{DEL}$) was developed. $PDFF_{DEL}$ describes the intraindividual difference between a typical WAT and a typical BAT depot and is calculated as the difference of $PDFF_{GLU}$ and $PDFF_{SC}$. The main and novel finding of this study was the significant correlation of $PDFF_{DEL}$ and CIT.

The reported significant correlation of $PDFF_{DEL}$ and CIT proves MRI measurements of the supraclavicular fossa can act as surrogate marker for CIT, as long as confounding adiposity is taken into account. Correction is especially relevant when overweight or obese patients, who would constitute the future area of application, are assessed. $PDFF_{DEL}$ and the role of BAT for human metabolism would need to be verified in larger prospective studies, but due to its reliability and noninvasiveness, the marker $PDFF_{DEL}$ could open up BAT research to a broader

spectrum of clinical application. Hereby, coming one step closer to using MRI for the assessment of BAT and the long-term goal to use BAT as possible treatment target for obesity and metabolic syndrome in daily clinical practice.

Please note, that the main findings of this work have been published as a first-authored journal article in Quantitative Imaging in Medicine and Surgery (QIMS).

2   List of publications

The following list shows topic related journal articles and conference papers I contributed to listed by the year of publication.

2.1   Journal articles

Held C, Junker D, Wu M, Patzelt L, Mengel LA, Holzapfel C, Diefenbach MN, Makowski MR, Hauner H, Karampinos DC. Intraindividual difference between supraclavicular and subcutaneous proton density fat fraction is associated with cold-induced thermogenesis. Quantitative Imaging in Medicine and Surgery. 2022;12(5):2877.

Drabsch T, Junker D, Bayer S, Wu M, **Held C**, Karampinos DC, Hauner H, Holzapfel C. Association between adipose tissue proton density fat fraction, resting metabolic rate and FTO genotype in humans. Frontiers in Endocrinology. 2022;13:804874.

2.2   Conference papers

Wu, M., **Held, C**., Diefenbach, M.N., Meineke, J., Mishre, A.S.D.S., Weiss, K., Kan, H.E., Junker, D., Hauner, H., Karampinos, D.C., Breathing-induced B0 fluctuations bias proton density fat fraction and T2* mapping of brown adipose tissue in the supraclavicular fossa, in: *Proc of 29th Scientific Meeting of ISMRM*. Virtual Conference, p. 3854. [digital poster] (2021)

Weidlich, D., Honecker, J., Ruschke, S., Patzelt, L., **Held, C**., Wu, M., Franz, D., Winkler, S., Hauner, H., Karampinos, D.C., Comparison of adipocyte size measurements with histology and high b-value diffusion-weighted spectroscopy in human white adipose tissue at 3 T, in: *Proc of 28th Scientific Meeting of ISMRM*. Virtual Conference, p. 4680. [digital poster] (2020) ISMRM Magna Cum Laude Merit Award

Held, C., Junker, D., Wu, M., Patzelt, L., Mengel, L., Hauner, H., Karampinos, D.C., Supraclavicular proton density fat fraction (PDFF) correlates with cold-induced thermogenesis in lean/normal-weight individuals, in: *European and International Congress on Obesity*. Virtual Conference, pp. EP-204. [digital poster] (2020)

Zhao, Y., Ruschke, S., Weidlich, D., Wu, M., **Held, C**., Doneva, M., Makowski, M.R., Menze, B., Karampinos, D.C., Water T2 relaxometry in fat-containing tissues using a T2-prepared Dixon-TSE sequence, in: *Proc. of ESMRMB 2020*. Virtual Conference, p. P01.17. [lightning talk] (2020)

Wu, M., **Held, C**., Patzelt, L., Weidlich, D., Ruschke, S., Mengel, L., Hauner, H., Franz, D., Karampinos, D.C., Brown adipose tissue water ADC quantification with Diffusion-Weighted MR Spectroscopy in the human supraclavicular fat, in: *ISMRM Workshop on MRI of Obesity and Metabolic Disorders*. Singapore. [oral presentation] (2019)

Franz, D., **Held, C**., Wu, M., Patzelt, L., Mengel, L., Rummeny, E.J., Hauner, H., Karampinos, D.C., Intraindividual difference between supraclavicular PDFF and subcutaneous PDFF is associated with cold-induced thermogenesis in adults, in: *ISMRM Workshop on MRI of Obesity and Metabolic Disorders*. Singapore. [oral presentation] (2019)

<u>Contents</u>

3 Introduction

Adipose tissue or body fat is a form of connective tissue, with very important tasks for human energy homeostasis and metabolism. Adipose tissue does not solely store excess energy for bad times, but also functions as a highly coordinated organ: Adipocytes, nerve tissue as well as stromovascular and immune cells work together as an intricate unit communicating via cytokines, hormones or nerve signals to achieve energy homeostasis [1]. Adipose tissue responds to triggers from the central nervous system and plays a vital role in hormone synthesis. In this sense adipose tissue functions as an endocrine organ central to human metabolism. Its importance is underlined by the impact adipose tissue accumulation or depletion has on human metabolic health, for example seen in patients with obesity or cachexia.

Adipose tissue accumulation, or rather obesity can lead to a symptom complex known as metabolic syndrome including hyperlipidemia, hyperglycemia, insulin resistance and hypertension, resulting in a proinflammatory and prothrombotic state [2]. This fosters cardiovascular disease, the number one cause of death worldwide, with rising prevalence in western societies as well as in developing countries [3, 4]. Cardiovascular disease accounts for roughly 17.9 million deaths per year worldwide [5] and obesity or even moderate degrees of overweight play a leading role in public health challenges [6].

Dominated by white adipose tissue (WAT), storing and releasing energy is one of the main functions of adipose tissue, but another form known as brown adipose tissue (BAT) combusts calories for heat production. BAT commonly occurs in rodents and hibernators, but also in human infants [7, 8], keeping them warm without the need of muscle activity. BAT is not only activated by cold exposure to maintain body temperature, but also contributes to metabolic homeostasis. Active BAT can reduce insulin resistance as well as hyperlipidemia [9, 10] and certain diets or rather nutrients seem to spark BAT activity.

As discussed, cold exposure sparks BAT activity [11] to maintain body temperature, by increasing human metabolism. A process called non-shivering thermogenesis in contrast to shivering-thermogenesis which is derived from muscle activity. Under cold exposure an estimate of up to 200-400 kilocalories (kcal) of daily energy expenditure is attributed to human BAT [12, 13]. This increase in daily calorie combustion under thermal challenges is measured by indirect calorimetry in relation to baseline as the so called cold-induced thermogenesis (CIT) [14]. CIT quantifies the individual's ability for endothermic thermoregulation and calorie combustion in BAT.

Both aspects, contribution to metabolic homeostasis and contribution to daily energy expenditure, render BAT a very promising treatment target for metabolic dysfunction, overweight and obesity.

However, due to its wide spread location alongside major vessels of the human body (mediastinal, paracervical, supraclavicular, parathoracic, supra- and perirenal) [8], BAT is hard to detect and its existence and activity in human adults was neglected for a long time. This changed when a series of studies using positron-emission tomography (PET) and biopsies [15-17] found supraclavicular and paravertebral glucose uptake could be derived from active BAT depots. Since then many different imaging techniques [18] for BAT characterization have been developed, with the most common being computer tomography (CT) and magnetic resonance imaging (MRI) techniques, often combined with PET and/or cold exposure. Big advantages of MRI are the lack of ionizing radiation, non-invasiveness, good spatial resolution, and the possibility for quantitative imaging. Moreover, MRI techniques measuring the fat-fraction [19, 20], based on the Dixon-method [21], open up possibilities for BAT detection independent of its activation. Fat-fraction techniques rely on compositional and morphological differences in the microstructure of WAT and BAT. Driven mainly by the water / fat content, the quantitative MRI parameter proton density fat fraction (PDFF) is calculated from water-fat separated images and quantifies adipose tissue composition. In humans, brown adipocytes are typically mixed with white adipocytes. An adipose tissue depot known for a higher BAT proportion like the supraclavicular fossa is accompanied by lower PDFF values compared to typical WAT regions.

3.1 Clinical relevance

The worldwide prevalence of overweight has doubled since 1980. Across all ages, both sexes and independent from the socioeconomic status, nearly one third of the world´s population has to be considered overweight [22]. The accompanying risk for cardiovascular disease opposes a burden for health care provision and public health in developed as well as non-developed countries. Therefore the world health organization (WHO) demanded that obesity must be considered as an independent disease and as a public threat calling for preventive measures around the globe and in all levels of societies [23]. In the center of all this stands the metabolic syndrome, with its main player the endocrine organ adipose tissue.

Active BAT is known to influence human energy homeostasis [24], regulate glucose homeostasis as well as insulin sensitivity [25, 26], and increase triglyceride clearance [9]. These

positive effects on metabolic homeostasis render BAT a promising treatment target for overweight and metabolic syndrome with an enormous potential. However, the gold standard for BAT detection is still PET-CT under cold exposure, which is time consuming, expensive, and possibly harmful (invasiveness, ionizing radiation). Further, BAT presence does not mean active BAT contributing to energy homeostasis and the functional assessment necessary to evaluate BAT activity is usually performed either by glucose-uptake of adipose tissue on PET or by investigation of an increasing energy expenditure under thermal challenges or rather CIT evaluation. However, the method of indirect calorimetry is far too time-consuming and costly for an application on a day-to-day basis in healthcare. Nowadays MRI applications find widespread use and become more popular, available, and thereby also cheaper. A reliable detection technique via the MRI parameter PDFF would open BAT research to a wider scope of clinical research. Moreover, if an association of MRI-based parameters and CIT could be verified, a simultaneous detection and functional evaluation of BAT via MRI would jumpstart the vision of metabolic phenotyping, individualized dietary interventions, or even pharmacological BAT activation as treatment for metabolic syndrome and obesity.

3.2 Hypothesis

CIT measurements provide information about the individual thermogenic capacity in response to cold and can be interpreted as functional assessment of the human BAT organ. MRI investigations conducted under static thermal conditions, however, give quantitative imaging information about composition and morphology of the investigated BAT depot. Therefore, the quantitative MRI marker PDFF can be depicted as descriptive compositional parameter.

Based on the hypothesis that the functional capacity of the BAT organ should be related to its composition, PDFF measurements of the supraclavicular fossa are expected to correlate inversely to CIT. Thus, the purpose of the study is to investigate the functional parameter (CIT) in association to the compositional parameter (PDFF), ultimately aiming to establish PDFF as possible surrogate marker for CIT in order to describe the individual thermogenic potential via MRI without the need of prior cold activation.

4   Theoretical background

4.1   Brown adipose tissue

Human adipose tissue can be subdivided in at least two different tissue types with different anatomy and function – WAT and BAT. Due to the intertwined functionality, with WAT storing energy and BAT burning energy, both tissues build a functional unit and adipose tissue can be classified as an organ [27, 28]. WAT stores excess energy in form of lipids and releases them into the bloodstream when needed. Thereby WAT compensates fluctuations in nutrient supply and guarantees steady energy homeostasis. Brown adipocytes are distinct for mammals and have likely developed 150 million years ago [8]. BAT uses the chemical energy stored in lipids for heat production and enables mammals to maintain body temperature, without the need of muscle activity. This is of great importance in hibernators and in human infants directly after birth.

4.1.1   BAT and WAT can be differentiated by cytology and immunohistology

The opposing functions of BAT and WAT are also reflected in adipocyte morphology. White adipocytes are spherical and quite big cells. A rather thin nucleus is pushed against the cell wall by a cytoplasmic unilocular fat droplet. Brown adipocytes are smaller polygonal cells, and instead of one large lipid droplet, they display multiple small droplets in their cytoplasm. The round nucleus lies centrally, and the dominant cell organelles are numerous iron rich mitochondria [8, 28]. The different morphology is displayed in Figure 1.
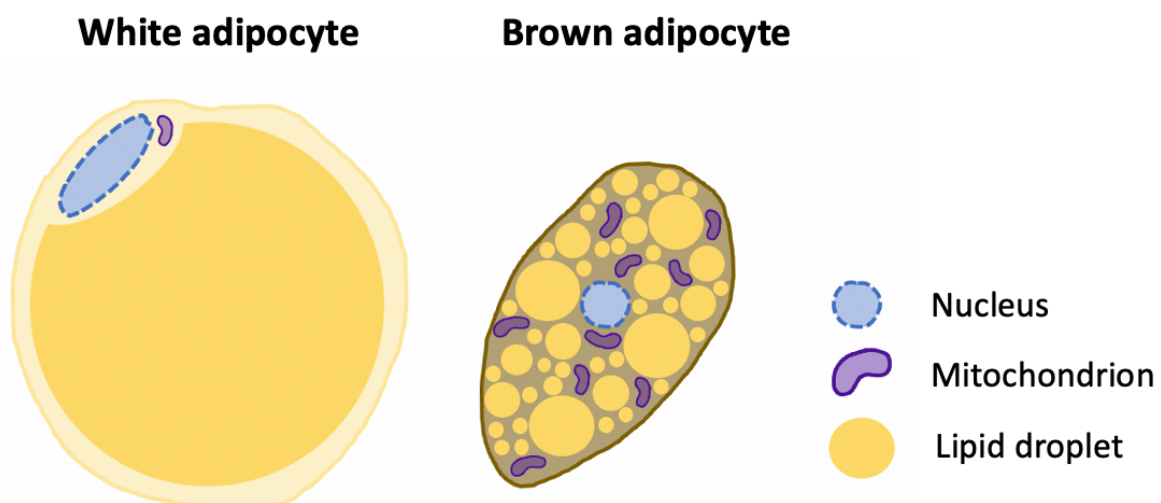

Figure 1: Schematic illustration of the different morphology of white (left) and brown (right) adipocytes.

With immunohistology both adipocyte types can be clearly differentiated. White adipocytes are immunoreactive for leptin and S100-B, whereas brown adipocytes are positive for uncoupling protein 1 (UCP1) [28] - a BAT distinct protein relevant for the heat production in the respiratory chain (see chapter 4.1.4 - BAT physiology and function).

4.1.1.1 The two types of BAT and the browning phenomenon

Some adipocytes show a morphology in between the two classic adipocyte phenotypes and are referred to as beige or brown–in–white (brite) adipocytes [29]. They display varying degrees of cytoplasmatic lipid droplets, and their function is very similar to classical brown adipocytes. However, classic brown adipocytes originate from Myf5-expressing progenitor cells, previously known as skeletal-muscle-specific progenitors, whereas beige adipocytes express a different gene signature [30]. Probably beige adipocytes transdifferentiate from WAT under certain stimuli, like long-term cold exposure or adrenergic triggering. The phenomenon is called browning and can increase an individual's potential of maintaining body temperature via non-shivering thermogenesis [31].

Generally beige and brown adipocytes perform the same physiological task and share a very similar morphology. A precise distinction was not considered necessary for this work and both adipocyte types will be jointly referred to as BAT.

4.1.2 The anatomical differences of human and rodent BAT

While human WAT is especially found in subcutaneous depots, BAT is not located in one particular region, but widely dispersed over the human body. It is mainly present in deep fat depots of the upper body (neck and axillae), around the kidneys and adrenals, paravertebral, and along large blood vessels of the mediastinum [32-34]. In infants BAT can also be found in a subcutaneous depot between the shoulder blades. Interestingly there are topological similarities to BAT depots in rodents. Rodents display BAT depots primarily in the interscapular region and the axillar region. Smaller depots are located cervical, paravertebral and in perirenal areas [35]. Consult Figure 2 to compare the different BAT depots in rodents and humans. Some speculate that the dispersed nature of BAT around large blood vessels and important organs is likely due to optimal thermal transfer, preserving vital functions under extreme thermal stress [34].
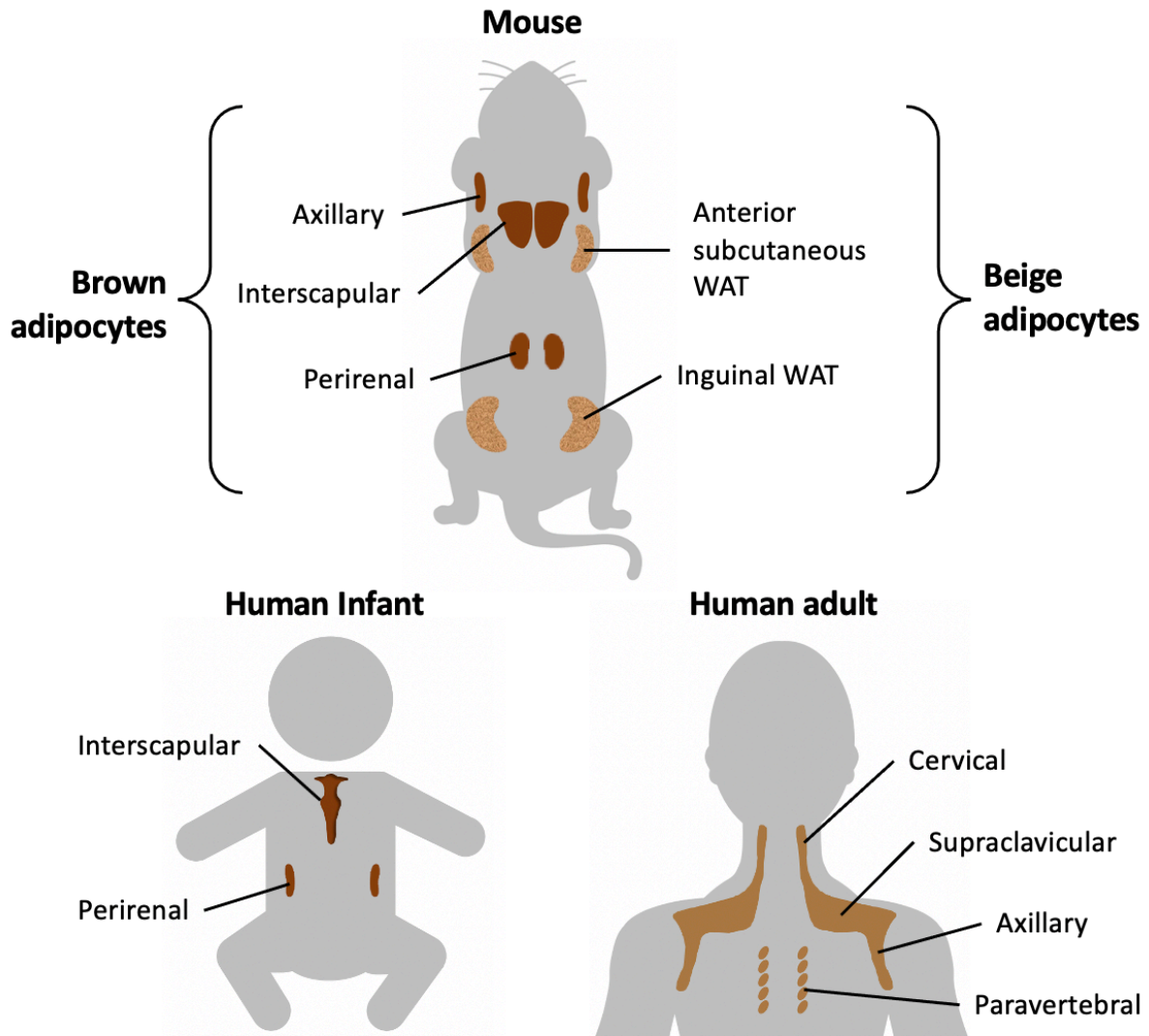
Figure 2: The different distribution of BAT, displayed in a mouse, a human infant, and a human adult. Note typical BAT depots are depicted in dark brown, WAT depots with embedded beige adipocytes found in rodents are depicted in a speckled light brown, and depots with coexistence of brown, beige, and white adipocytes typically found in the supraclavicular fossa of human adults are depicted in light brown. BAT, brown adipose tissue, WAT, white adipose tissue.

From a physiological perspective (mitochondrial UCP1 function) human and rodent BAT have similar nature and function [36, 37], which explains the major role rodents play in BAT research. However, comparability is vigorously discussed [38]. Adult human BAT is widely dispersed and often differs from classic BAT on a cellular level. Typical human BAT depots are often a mixture of brown, beige and even white adipocytes [29, 39], while typical BAT depots in rodents (interscapular, axillary) are homogenous and dominated by classic brown adipocytes [40].

4.1.3   The supraclavicular fossa as region of interest in BAT research

A number of autopsies by Juliet M. Heaton in 1972 [32] delivered detailed description of BAT locations and their deterioration with ageing. After the first decade, the involution of BAT into WAT renders BAT depots more and more indistinguishable from WAT, until they are nearly gone by the age of 80. In particular, subcutaneous BAT found in a thin layer between the shoulder blades and in the abdominal wall, vanishes after the first ten years of life [32]. Consequently, metabolically active BAT was predominantly associated with infants and children, until multiple reports from the field of nuclear medicine found signs of active BAT in adults in the early 2000s. On ^{18}F-fluorodeoxyglucose (FDG) -PET scans, routinely conducted in metastatic cancer patients, tracer accumulation in the upper body was repeatedly described [33, 41] and could not be explained by neoplasia. The glucose uptake was found cervical, supraclavicular, mediastinal, paravertebral and suprarenal [33] and corresponded to the known BAT locations. After that a series of high ranking FDG-PET studies published in 2009 followed, finally proving the continued existence of active BAT in adults [15-17].

The dispersed nature of the human BAT organ complicates consistent and reproducible research. With major blood vessels passing through the supraclavicular fat depot and in combination with the pronounced glucose uptake [42], the supraclavicular fossa quickly became the main region of interest (ROI) in BAT research. The supraclavicular fossa is superficially located, better accessible and less affected by breathing motion compared to other BAT locations such as the region around the adrenal glands. All of that can be important for the different imaging modalities used in BAT research, like multispectral optoacoustic imaging (MSOT), infrared thermography, or quantitative MRI. Consequentially, the supraclavicular fossa is the main location investigated by radiological studies of BAT.

4.1.4   BAT physiology and function

Two main roles have been suggested for BAT. Firstly, the response to cold and the task of maintaining a stable body temperature. Additionally, an increase in BAT activity was observed as a response to certain diets, indicating a second function of BAT: maintaining metabolic homeostasis when a surplus of caloric energy occurs. Either way calories are combusted and heat is produced, therefore the tasks are called thermoregulatory thermogenesis and metaboloregulated thermogenesis [8]. Whereas the purpose of thermoregulatory thermogenesis is straightforward and probably the main biological role, BAT activity being sparked by high calorie diets has been discussed controversially [43]. In the present work, thermoregulatory

thermogenesis referred to as CIT is mainly considered. The physiology of thermogenesis is explained hereinafter.

4.1.4.1 UCP1 uncouples the respiratory chain from adenosine triphosphate (ATP) synthesis and produces excess heat

The above-mentioned protein UCP1 is found in the countless mitochondria of brown adipocytes and responsible for their specific operating principle. The cristae of mitochondria serve as site for the respiratory chain, where the chemical energy stored in lipids is harvested and used for adenosine triphosphate (ATP) synthesis. Therefore, the chemical bonds are broken up in the respiratory chain and with this energy, a proton gradient over the inner mitochondrial membrane is created. The process requires oxygen (O_2) and produces carbon dioxide (CO_2) as a waste product. Normally the gradient is utilized by the ATP-synthase and the energy is rebound in the tri-phosphate bond of the body's energy currency - ATP. However, in brown adipocytes UCP1 creates a short circuit over the inner mitochondrial membrane and the protons flow back freely. As a result, the excess energy is released as heat [44].

4.1.4.2 The metabolic importance of BAT

Activated BAT combusts calories and increases energy expenditure. Studies found improved weight control and lower BMI in adult human beings with active BAT depots [15, 16, 33, 42]. However, it is controversially discussed how large the effect of active BAT on energy expenditure really is and the numbers in the literature vary between 1 - 20% increase [45]. But even if the contribution to energy expenditure is minor and thereby possibly not of great relevance for weight loss, data suggests the importance of active BAT for human metabolic health. It was found that cold activated BAT increases glucose uptake and whole-body insulin sensitivity, and the glucose uptake in BAT was found to be lower in individuals with obesity and / or diabetes [46, 47]. Additionally, BAT can effectively improve triglyceride clearance and regulates lipoprotein cholesterol levels [9]. The central role in human metabolic homeostasis points towards BAT as a possible treatment target in metabolic syndrome and obesity. Cold- or pharmacologically activated BAT could possibly treat overweight and obesity, reduce metabolic risk factors and cut cardiovascular disease [48].

4.1.5 Cold exposure and energy expenditure

Human body weight is lastly determined by energy intake and energy expenditure. The average human energy expenditure is largely composed by physical exercise plus a baseline called basal metabolic rate (BMR) or resting energy expenditure (REE). Basically, REE describes the amount of energy the human body and organs need to maintain basic cellular metabolism and vital function, while the body is at rest. REE is dependent upon factors such as body height, body weight, muscle mass, genetics, and gender. The term BMR is often understood as the measured REE without other influencing factors. Exemplary influencing factors are changes in environmental temperature, like cold exposure or psychological stress. Both can raise REE. Table 1 shows REE determinants [49].

Table 1: Determinants of resting energy expenditure in humans.

Increased REE	Decreased REE
Cold exposure	Prolonged fasting
High altitude	Drugs: Sedatives, Beta blockers
Exercise	
Pregnancy and lactation	
Ethnicity (Caucasian)	
Hormones: Thyroid, Glucagon	
Psychological stress	
Fever and illness	

REE, resting energy expenditure.

The increase in REE under cold exposure is derived from BAT activity and when shivering occurs additionally from muscle activity. Thus, in experimental settings, in order to measure solely the energy uptake from BAT, temperature is kept above the individual's shivering threshold. The resulting increase in calorie combustion compared to baseline constitutes the CIT, sometimes also referred to as non-shivering thermogenesis. CIT is used as a measure for BAT activity [14].

CIT is mainly controlled by the sympathetic nervous system (short-term) and thyroid hormones (long-term) [45]. Those pathways regulate the acute response to cold and the adaptation of the tissue, by the means of proliferation versus atrophy of brown adipocytes. For the present study, only short-term effects of cold exposure were investigated, thus especially control mechanisms via norepinephrine are of interest.

4.1.5.1   Norepinephrine controls short term BAT activity under thermal challenges

From rodent studies we know that brown adipocytes express all types of adrenergic receptors. The β-adrenergic pathway is the best studied and especially β3-stimulation seems to be responsible for BAT thermogenesis. The β3-receptors are almost only found in WAT and BAT. Therefore, it is concluded that the energy expenditure increase observed under stimulation with specific β3-agonists, can be attributed solely to active BAT [44]. In short, cold exposure triggers the sympathetic nervous system and consequentially norepinephrine signals lead to an increase in BAT activity, with raised calorie combustion and heat production.

4.1.5.2   Measuring resting energy expenditure with indirect calorimetry

As mentioned above, in the human body energy is gained from chemical energy stored in carbon-based nutrients. The energy is extracted by oxidizing the substrate to CO_2 and water under O_2 consumption and with heat as a byproduct [49]. Average REE can be calculated from CO_2 output volume (VCO_2) and O_2 consumption volume (VO_2), by using the modified Weir equation [50]. The simplified version, mostly used, neglects the urinary Nitrogen component which is maximally responsible for 4% of REE.

$$REE \left(\frac{kcal}{day}\right) = \left((VO2 \times 3.941) + (VCO2 \times 1.11)\right) \times 1440$$

The fundamental principle of indirect calorimetry is to measure VO_2 and VCO_2 for the calculation of REE in kcal per day.

4.2   Magnetic resonance imaging

Many achievements of modern medicine are founded in medical imaging. Looking into a body without hurting it, provides so many opportunities: From diagnosing broken bones via X-ray, over detecting intracranial bleeding on a CT-scan, to observing tumor growths with MRI - the fascination of medical imaging remains unhindered. MRI is especially interesting; hence it can map all kinds of tissues, without any negative side effects like harmful radiation. When the right techniques are chosen, a special tissue of interest, like adipose tissue, can be enhanced, or running fluid such as blood, can be investigated in an MR-angiography. The possibilities are

endless. In the following the physical principle behind the nuclear magnetic resonance phenomenon will be explained very briefly. For detailed description please refer to scientific key literature [51]. Hereinafter the rationale behind the techniques used in this work is depicted.

4.2.1 MRI basic principle

The human body, as well as all matter, is made of atoms. Atoms contain electrons and protons with electric charge as well as neutrons without electric charge. The atoms' nucleus holds the neutrons and protons and can be described by four important physical properties: mass, electric charge, magnetism, and spin. When imaging biomatter, especially hydrogen (H) or rather the protons of hydrogen (^{1}H), are of interest. First due to their universal presence and second due to their magnetic potential. The uneven electrical charge of ^{1}H is responsible for its magnetism and combined with the natural property spin, ^{1}H behaves like a small rotating rod magnet (Figure 3a).
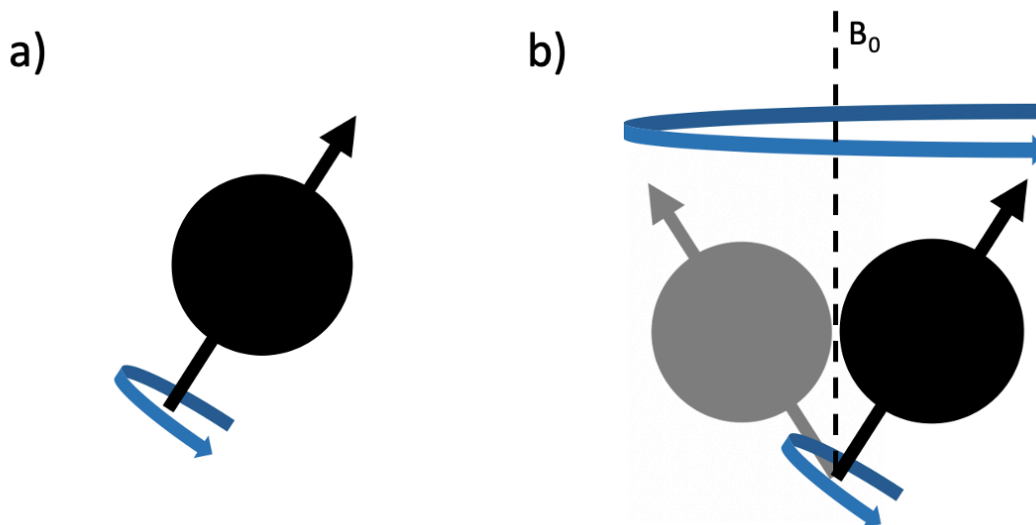
Figure 3: Illustration of ^{1}H with natural spin, behaving as a rod magnet and rotating around its own axis (3a). ^{1}H with natural spin and precessing around the magnetic field B_0 (3b). B_0, main magnetic field; ^{1}H, proton of hydrogen.

The magnetic orientation is under natural conditions random and described by a vector (Figure 4a). When placed into a strong magnetic field (B_0), the vectors show primarily two orientations, parallel or anti-parallel with B_0 (Figure 4b). Hereby the proportion of parallel aligned nuclei outweighs the proportion of anti-parallel aligned nuclei, creating a net-magnetic moment (M) parallel to B_0.

11

Figure 4: Schematic illustration of ^1H a) in no magnetic field showing random orientations and b) in strong magnetic field B_0 oriented parallel or antiparallel to B_0 (grey arrows). Note, the majority of ^1H is oriented parallel to B_0. B_0, magnetic field; ^1H, protons of hydrogen.
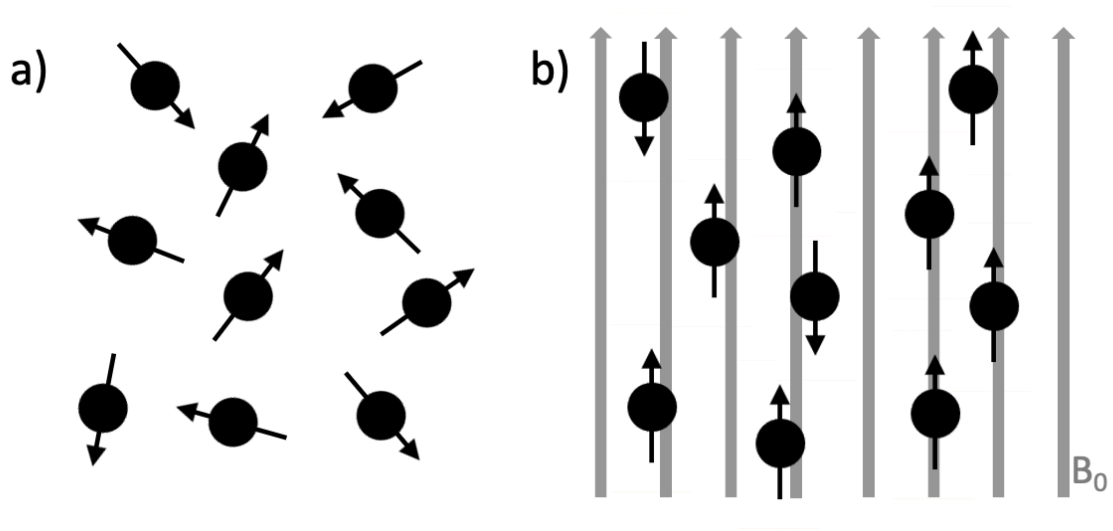
Additionally, the aligned ^1H nuclei precess out of phase around the direction of B_0 (Figure 3b). This behavior is called Larmor precession, with the Larmor frequency (ω) proportional to the magnetic field strength (B_0) and the gyromagnetic ratio (γ). γ is a tissue specific constant.

$$\omega_0 = \gamma\, B_0$$

The described state is perceived as equilibrium of the examined object and its behavior in B_0.

For obtaining MR images, the object is excited with a radio frequency pulse (RF) perpendicular to B_0. This forces all vectors, and therefore the vector M, to tilt away from B_0, and leads to the reduction of the longitudinal component of M. The RF pulse is applied in the specific frequency of the gyromagnetic ratio of the tissue and molecule of interest. In medical imaging the target nucleus is almost always ^1H, except for special research applications. Vectors start precessing in phase, creating a new transversal component of M.

When the RF pulse is turned off, the excited tissue returns to equilibrium. The longitudinal component of M increases again, whereas the transversal component decays until equilibrium is reached. This is called relaxation and during relaxation excited nuclei emit energy in form of

a measurable RF. The signal is named free-induction decay (FID). FID is proportional to the proton density of a tissue - the more protons, the stronger the FID.

The time needed for relaxation is different based on the tissue. Measured relaxation time is responsible for gray scale intensity in MR images. In classical MR images two specific parameters are measured. First the relaxation time a specific tissue needs until the return of the longitudinal component of M (T_1) and second the relaxation time needed until the full decay of the transversal component of M (T_2). During acquisition, RF pulses are repeated in a predetermined time – called repetition time (TR). At any time between two RF pulses, the FID response can be measured, and the chosen time is called echo time (TE). The adjustment of TR and TE leads to very different image contrast and is thus used to accentuate different tissue types.

The principle of gradients used to encode the FID signal for each dimension, as well as the need of Fourier's transformation to decode measured signals will not be further discussed here for the sake of simplicity.

4.2.2   Quantitative MRI in metabolic imaging

The MRI can be used as a simple imaging device, creating a grey scale map. The map can be evaluated by clinicians and researchers and allows qualitative interpretation like categorization and comparison.

Consequentially just "taking pictures" with the MRI could be referred to as qualitative MRI, where the units of the measured pixel correspond to an arbitrary scale and pixel values within an image can be only compared relative to each other but not across images. In quantitative MRI, the MRI scanner is instead used as precise scientific measuring instrument. Results are not only depicted in gray scale but correspond to a mathematical value in an absolute measuring scale with meaningful units that enable comparison of the pixel values across images. Those quantifications allow the application of basic scientific quality principles like reproducibility and validity on MRI research. The expectation is that the MRI measures are accurate and a consistent reflection of reality and could be repeated anytime with the same outcome. This enables researchers to collect data, compare it, and statistically evaluate it. In a broader sense quantitative MRI means the implementation of MRI as a measuring device [52]. Hence, quantification is defined as measuring the number, the amount, or the size of something, with the possibility to express the result in numeric value [53].

In the field of metabolic imaging, this capacity is used for the further understanding of metabolic diseases, evaluating prognoses, and verifying treatment effectiveness. For the current exploration, metabolic imaging methods of interest are fat quantification methods, like the signal fat fraction (SFF) and especially the PDFF.

4.2.3 Quantitative MRI and fat quantification

In contrast to other imaging modalities, MRI shows very good soft tissue contrast. The underlying MR-physics concept exploited, is that protons bound in different molecules exhibit different resonance frequencies. For example, protons in water show very different resonance frequencies and T_1/ T_2 relaxation times, compared to protons bound in triglyceride molecules. Specific capacities can be exploited for either fat suppression, if underlying pathologies are of interest, or for fat accentuation. The latter is mostly used for fat quantification purposes. Two different strategies are pursued, if the separation of water and fat signals is of interest [54]. For fat-suppression techniques, a special selective water excitation pulse is used, or a combination of RF pulse and gradient pulse to excite and then saturate fat signal prior to the excitation of water. The aim is to suppress the excitation of protons bound in triglycerides compared to protons in water and thereby suppressing the fat signal. To generate water-fat separated images with this method, the acquisition of two imaging sets with the exact same imaging modalities, with or without fat suppression pulses, is needed. Chemical-shift based techniques obtain the water-fat separation in postprocessing and enable the simultaneous acquisition of water-only and fat-only images. The approach was originally published by Dixon in 1984 [21] and ever since, the Dixon-technique is the base for multiple new imaging sequences. The basic principles are explained below.

4.2.3.1 Water-fat separation with the Dixon method

The Dixon method relies on chemical-shift differences of water and fat, known from simple magnetic resonance spectroscopy (MRS). In MRS, the measured resonance frequencies of a voxel are fully encoded and resolved in the displayed spectrum. As mentioned above, protons bound in different molecules display different resonance frequencies. The variation compared to an arbitrary chosen standard is called chemical shift and is specific for different molecules. Causative are electrons shielding the atomic nucleus and influencing its magnetic property. The Dixon method assumes that water and fat are the two dominant components of the returned MR

signal, with other components being negligibly low. Traditionally, Dixon data is acquired for two different TEs. TEs are specifically chosen to first measure water signal (W) and fat signal (F) in-phase (IP) and secondly in 180° opposed-phase (OP). Simple summation and subtraction of the two images, allows calculation of water-fat separated images:

$$1) \quad IP = W + F$$
$$2) \quad OP = W - F$$

From 1) and 2) water-only and fat-only images can be calculated like:

$$3) \quad W = \frac{1}{2} \times |\, IP + OP \,|$$
$$4) \quad F = \frac{1}{2} \times |\, IP - OP \,|$$

Note that the equations are simplified. The calculation of error phase due to field inhomogeneity or system imperfection is neglected since it is not important for basic comprehension.

4.2.3.2   Multi-echo Dixon

In the last decades, several Dixon methods have been developed, mainly characterized by the acquired numbers of echoes, also called points. Development of multi-echo acquisition methods gradually allowed more flexible choice of TE, no longer restricted to in-phase and opposed-phase TEs. Facilitating flexible sequence design and thereby achieving shorter scan times, higher resolution, and better signal to noise ratios.

4.2.3.3   The principles of calculating tissue fat fraction

Fat fraction techniques were initially developed to measure liver fat for non-invasive assessment of hepatic steatosis. But application spread in all different regions of metabolic imaging including adipose tissue imaging, using SFF or rather PDFF measurements. For the calculation of SFF, water-fat separated images are used and the signal from fat (F) is divided by the combined signal from water (W) and fat.

$$SFF = \frac{F}{W + F} \times 100$$

Consequently, every voxel is described by a numeric value between 0 and 100 expressed in % and describes the signal proportion attributed to the fat component of the voxel. The SFF is known to be influenced by an abundance of biological, physical, and technical confounding factors and is thus not considered particularly accurate. The known confounding factors are listed below [54]:

1. T_1-bias
2. T_2* decay
3. Spectral complexity of fat
4. Noise bias
5. Eddy currents
6. J-Coupling
7. Field inhomogeneities

Advanced MRI techniques addressing the confounding factors above allow the calculation of PDFF. Note that in contrary to SFF, the PDFF expresses the signal proportion attributed to mobile protons of fat in a voxel. Currently, PDFF is the most useful and most reliable marker to express tissue fat proportions [55]. PDFF is considered an unconfounded biomarker and in 2012, an informal agreement was made in the MR community to use PDFF as the standard MR-based quantifying method of tissue fat proportions [55].

4.2.4 Quantitative MRI in BAT research

Under 4.1.1 explained morphological differences of BAT and WAT, lead to different MRI characteristics and the possibility to differentiate between the two, with the help of quantitative MRI. Commonly used markers for BAT research are PDFF and T_2-star (T_2*) relaxation time, which are discussed hereafter.

4.2.4.1 PDFF- a marker to detect the lower fat proportion in BAT

With numerous mitochondria and smaller lipid droplet size of brown adipocytes, as well as with dense vascularization of BAT, the pure fat proportion is lower in BAT compared to WAT. Thus, significantly lower PDFF in BAT than in WAT depots, have been reported in several publications [56-60]. Additionally, a couple of studies not reporting on PDFF but SFF, detected similar differences [61-63]. Most fat fraction values reported for BAT are between 50% and 90%. But it is very important to consider the dependency of results on different postprocessing methods: (1) Do the reported values refer to a small manually placed ROI or the whole BAT depot e.g., the supraclavicular fossa? (2) Was a threshold applied and which cut off values were chosen? (3) How large is the impact of partial volume and did the exploration try to reduce it e.g., by erosion? (4) Was the examined BAT inactive or activated, for example were measurements performed at ambient temperature or under thermal challenges?

PDFF is a robust, reproducible and accurate measure for tissue fat content [55] and combined with the results above, this indicates PDFF as suitable marker for BAT. However, in adipose tissue, individual PDFF is known to be strongly associated to body composition [64]. This means that the PDFF of pure WAT in two individuals can differentiate significantly from another, depending on their body adiposity. That is why correct measurements of body composition and body adiposity, were a large part of the present study. The details of measuring body adiposity are discussed in chapter 4.3.

4.2.4.2 Measuring the different adipose tissue microstructure of BAT with T_2^* or R_2^*

T_2 is defined as the time needed for the decay of the transverse magnetization. The observed relaxation time in an in-vivo Dixon MRI experiment, is much smaller than anticipated from the model. This actual observed T_2 is called T_2^* ($T_2^* < T_2$). T_2^* effects include T_2 decay effects and effects from microscopic field inhomogeneities within the tissue. T_2^*-weighted images are popular to accentuate local microscopic field inhomogeneity and are used for measuring endogenous iron concentration. BAT displays an inhomogeneous microstructure and contains a lot of iron-rich mitochondria, thus T_2^* measured in BAT is significantly shorter than in WAT [57, 58, 60, 65, 66]. Note that some studies report R_2^* values, which describes the reciprocal value of T_2^*. Accordingly, reported R_2^* values in BAT are higher than in WAT. Results for BAT T_2^* are widespread and should be interpreted with care: Firstly, T_2^* mapping in adipose tissue is relatively new and there is little knowledge about its accuracy and reproducibility. Secondly a recent study found a strong association of adipose tissue T_2^* values to the number

of acquired echoes: T_2^* mapping in adipose tissue showed significantly smaller standard deviations and range with 20 acquired echoes compared to 6 echoes, thus using a higher number of echoes for T_2^* mapping in adipose tissue has been recommended [66]. This explains at least partly the wide range of reported T_2^* BAT values. With a higher number of acquired echoes and therefore an improved accuracy, T_2^* or R_2^* are promising BAT markers, exploiting differences in microscopic tissue texture.

4.3   Measuring body adiposity

For this study, body adiposity is not only relevant due to possible targeting of BAT as a treatment option for obesity, but also due to the dependency of the MRI biomarker PDFF on individual adiposity. A sufficient and reliant marker depicting the individual degree of obesity, was needed here for statistical correction of the results. In this chapter different markers for body adiposity are presented and respective advantages and disadvantages are discussed.

As already discussed before, the prevalence of obesity increases rapidly all over the world and in 1997 the WHO declared obesity a global epidemic. The sheer scale of the problem represents a great challenge for public health and health care providers. To tackle the enemy up against unification of research and treatment options was needed. Thus, a classification system via BMI cutoffs was recommended by the WHO, and by now it is widely used by researchers and clinicians to grade body adiposity. The BMI is a very easily assessed, but a crude marker. It does not account for individual variation of overweight, like body fat proportion, distribution, or body composition [67]. Additionally, with hard cutoff values, false classification can always happen and when interpreted on an individual, but not population-level, this can mean misinterpretation of data. Other, but more complex methods provide better depiction of individual body adiposity. Those measures are often more meaningful descriptions of an individual's nutritional status. The pros and cons of some measures for body adiposity are evaluated below.

4.3.1   Measuring body composition

In metabolic research, body composition often means the proportion of fat and non-fat mass in the human body. A relatively low amount of fat mass compared to non-fat mass is considered healthy and measurements for body composition are generally used to assess the individual fitness levels. The WHO considers the following tools suitable for the assessment of body

composition: BMI, waist circumference, under water weighing, dual energy X-ray absorption (DEXA), isotope dilution, body impedance analysis (BIA), and skinfold thickness [23]. The expense, cost, and the explanatory power of the methods vary widely. Often used tools like DEXA and BIA measure the fat proportion of the body, whereas the BMI or skinfold thickness are just approximations or rather indicators. But BIA and DEXA for example are quite complex, while the BMI is certainly the most cost-effective tool. The challenge remains keeping the balance between complexity of the measuring method and its meaningfulness. In the following, BMI and BIA will be opposed in its effectiveness as a measure for individual body composition, when information about the individual nutritional status is needed like in the present study.

4.3.1.1 BMI- a great measure on a population scale basis with poor diagnostic performance and sensitivity on an individual level.

The BMI is calculated from body weight in kilograms (kg) and body height in meter (m) squared (kg/m^2). It allows a classification and quantification of obesity, besides its relatively loose definition, as abnormal fat accumulation impairing physical health (WHO). In the classification different degrees of body adiposity are distinguished like underweight, normal weight, overweight and three classes of obesity. An overview of the WHO recommended BMI cutoffs is given in Table 2.

Table 2: BMI cutoffs for overweight and obesity classification recommended by the WHO.

Classification	BMI values in kg/m^2
Underweight	<18.5
Normal	18.8 - 24.99
Overweight	≥ 25
Obesity °I	30 - 34.99
Obesity °II	35 - 39.99
Obesity °III	≥40

BMI, body mass index; kg, kilogram; m, meter; WHO, world health organization.

Defining overweight by BMI, enables global comparison in research and provides a base to establish treatment and intervention options. Further it can be used as an effective screening tool. People at risk for higher morbidity or mortality are easily identified due to their high BMI values. The big strength of the BMI poses the ability to quickly estimate prevalence of obesity in different populations or subgroups. This creates an overview, ideal for epidemiological

studies. But there are downsides: The BMI does not account for regional distribution of body fat, nor does it distinguish between weight based on muscle mass or weight based on fat mass. That is why the relation of BMI values and actual body fatness varies dependent on body composition, age, sex, and ethnicity and if only BMI values are considered, they should be corrected accordingly [23]. Studies comparing the diagnostic performance of BMI to gold standard measurements of body fat percentage (BF%) suggest a poor accuracy when obesity is identified by BMI only [68, 69]. Results showed a good specificity of BMI cutoffs, but a poor sensitivity. More than 50% of the individuals were not labeled obese by BMI, whereas they should be considered obese due to their high BF%. Those results indicate major limitations of the universal gold standard definition of obesity with the possibility, that the prevalence and even the extent of the obesity epidemic are largely underestimated [69]. To sum up, the BMI is a good measure on a population scale basis but is unsuitable if information about the individual body fatness is needed.

4.3.1.2   Body impedance analysis (BIA) a tool for the assessment of individual body adiposity

BIA is a method using the different electrical property of tissues and the very fundamentals are explained in the following. Different tissues can act as a conductor or semi-conductor, in various degrees. For example, lean tissues with lots of water and electrolytes are highly conductive, whereas fat is a poor conductor. This is called specific resistivity (ρ). When body composition is assessed with BIA, an electrical but painless current is applied via four electrodes which are placed on wrists and ankles. The resistance of the material is measured, and from that the volume (V) can be calculated, by taking a model where the body is depicted as five cylinders (Figure 5), as a basis.
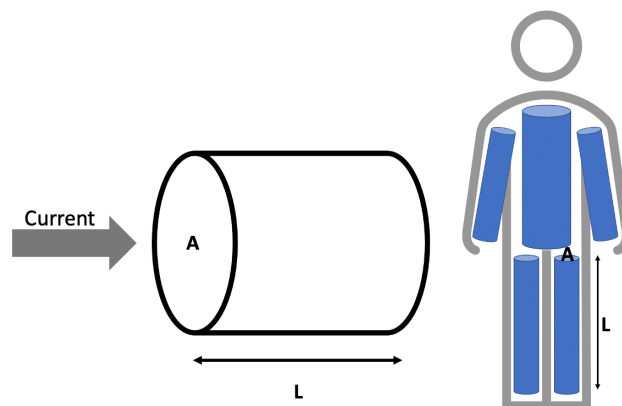

Figure 5: A model of the human body of five homogenous cylinders (right) is used as approximation. The volume of each cylinder can be calculated from its length (L) and area of cross section (A). For BIA an electrical current (grey arrow, left) is applied and the resistance R is measured for each cylinder. A, area of cross section; L, length; R, resistance.

For each cylinder the underlying physics principle- that the resistance (R) of a homogenous material is proportional to its length (L) and inversely proportional to its cross section (A)- is utilized [70].

$$R = \frac{pL}{A} = \frac{pL^2}{V} \qquad \text{and} \qquad V = \frac{pL^2}{R}$$

Complex equations taking body height, weight, and multiple other influencing factors into account, allow the calculation of body fat mass in kg. Further, the ratio of fat mass and body weight provides another important marker for body adiposity – the BF%. In contrast to the BMI, the BF% is an actual measure for body fatness and therefore a direct marker for obesity, not just an indicator. But the assessment of body composition with this method is prone to error. The most important source for errors, is the right application of these equations: Body shape, proportion, hydration status, and electrolyte levels can change drastically based on ethnicity, age, physical fitness, and gender. Those variations will alter BIA results significantly and must be considered when BIA is applied. On the other hand, indisputable advantages of BIA are its non-invasiveness, the possibility of rapid processing, its easy handling, and despite of purchasing the device its inexpensiveness. The reputation of inaccuracy of BIA roots in non-expert application in the fitness sector, where often just bipolar devices and probably improper equations are used. But if tetrapolar devices are used [71] and if the right equation for the assessed population is chosen [72], BIA can be a useful tool to evaluate body composition [71, 72]. However, it is extremely important to be aware of the population dependency, wherefore BIA lacks accuracy in large epidemiological studies with diverse populations [72]. If applied with care in smaller cohorts, BIA holds far more detailed information about actual body fatness and physical health than approximations like the BMI. With proper use BIA is considered a powerful tool for body composition assessment.

4.3.2 Detailed assessment of body composition and body fat distribution

The markers introduced so far, are measures or rather approximations for the total adipose tissue of an individual. By the WHO definition this is sufficient enough for the classification of overweight and obesity. But extensive research has shown that not just the total amount of body fat, but its distribution is of great importance for individual metabolic health. Especially central fat accumulation is known to be an important metabolic risk factor, increasing the risk for

21

metabolic syndrome and cardiovascular diseases. In metabolic research, different compartments of adipose tissue are differentiated: First there is visceral adipose tissue (VAT) which is made up of the adipose tissue around central organs and in the abdominal cavity and thorax. Secondly, fat depots just beneath the skin are called subcutaneous adipose tissue (SAT). Total adipose tissue results from the sum of VAT and SAT. Studies have shown that both VAT and SAT are strongly associated with metabolic risk, but VAT resulted to be a stronger predictor of metabolic syndrome and cardiovascular disease [73, 74]. There are approximate markers for central obesity, by the means of anthropometric measurements, like the waist to hip ratio or waist circumference, which do correlate with metabolic risk [75], but MRI offers a far more advanced assessment of body fat distribution [76].

4.3.2.1 Measuring adipose tissue distribution and volumes using MRI

When measuring body fat distribution with MRI, the main goal is creating good contrast between adipose and non-adipose tissue. This is usually done by T_1 weighted sequences or nowadays with the already discussed water-fat separated images derived from the Dixon method [77]. Both methods allow the exact distinction of adipose tissue, muscle, and other human tissue. By manual or semi-automatic segmentation, volumes and the regional distribution of non-adipose tissue, SAT, and VAT are precisely differentiated and quantified [76]. Nevertheless, MRI application remains costly and time consuming, but rapid full body scans developed over the last year were able to reduce scan time dramatically. Another problem is the complexity of the segmentation process. More and more possibilities for automatic post-processing are developed and a lot of the segmentation work is nowadays done by algorithms, but almost always time-consuming manual correction is required. A possible solution are automatic segmentation tools based on machine learning and trained with huge databases, hopefully enabling assessment without the need of manual correction in the future. However, so far segmentation is still the hurdle to overcome, when measuring body fat distribution. Apart from that, MRI can be considered the most powerful and especially most accurate non-invasive tool in body composition profiling.

4.3.2.2 Calculating body fat percentage from MRI

When total adipose tissue and total body volume are quantified, it also enables the calculation of a MRI based BF%, as the of total adipose tissue volume and total body volume. Although

this method is far more complicated and more expensive than BF% assessment with BIA, it can be used to validate BIA measurements [71]. If the agreement of BIA and MRI is high, the accuracy of BIA measurements can be counted on.

5 <u>Material and methods</u>

5.1 Study design

The explorative cross-sectional study was conducted in two phases at the Technical University Munich (TUM) in cooperation of the Else Kröner-Fresenius-Zentrum ZIEL-Institute for Food and Health (Freising-Weihenstephan, Germany), the Institute of Nutritional Medicine of TUM (Munich, Germany), and the Department of Interventional and Diagnostic Radiology of TUM (Munich, Germany). In the first study phase healthy adult volunteers in Munich and Freising were recruited via bulletin and university mailing lists. From October 2016 to January 2020 healthy, adult, and caucasian applicants were screened for the following exclusion criteria: smoking, unstable body weight (>3kg change in body weight over the last three months), excessive physical activity (>10 hours of demanding training per week), breast feeding, or pregnancy. If eligible, volunteers were examined in one of two study centers, either in Freising or Munich. During this first full day visit anthropological measurements and indirect calorimetry measurements were conducted, thus CIT values and anthropological measurements used in this investigation were generated in the first study phase.

In a second phase from March 2019 to January 2020, all participants of phase one with complete datasets were screened for the standard contraindications of MRI and invited via mail for additional MRI examination at the Department of Interventional and Diagnostic Radiology of TUM. The time frame varied widely, with appointments of phase one and two being a couple of days to a couple of months apart. In total, 184 participants were recruited in phase one, of whom 40 underwent additional MRI examination.

All participants gave written and informed consent before examination. The study protocol was approved by the Ethics commission of the Faculty of Medicine of Technical University Munich and both study phases are registered as separate studies at the German clinical trials register (DRKS); phase 1 (DRKS00010489) and phase 2 (DRKS00016629).

Anthropometric measurements and indirect calorimetry with the following variables were gathered in the first phase: age, weight, height, BF% and CIT, whereas all MRI data, PDFF and T_2* values as well as the adipose tissue volumes SAT and VAT, were collected in the second study phase. A detailed flow chart illustrating the recruitment process and timing of acquired parameters is displayed in Figure 6.
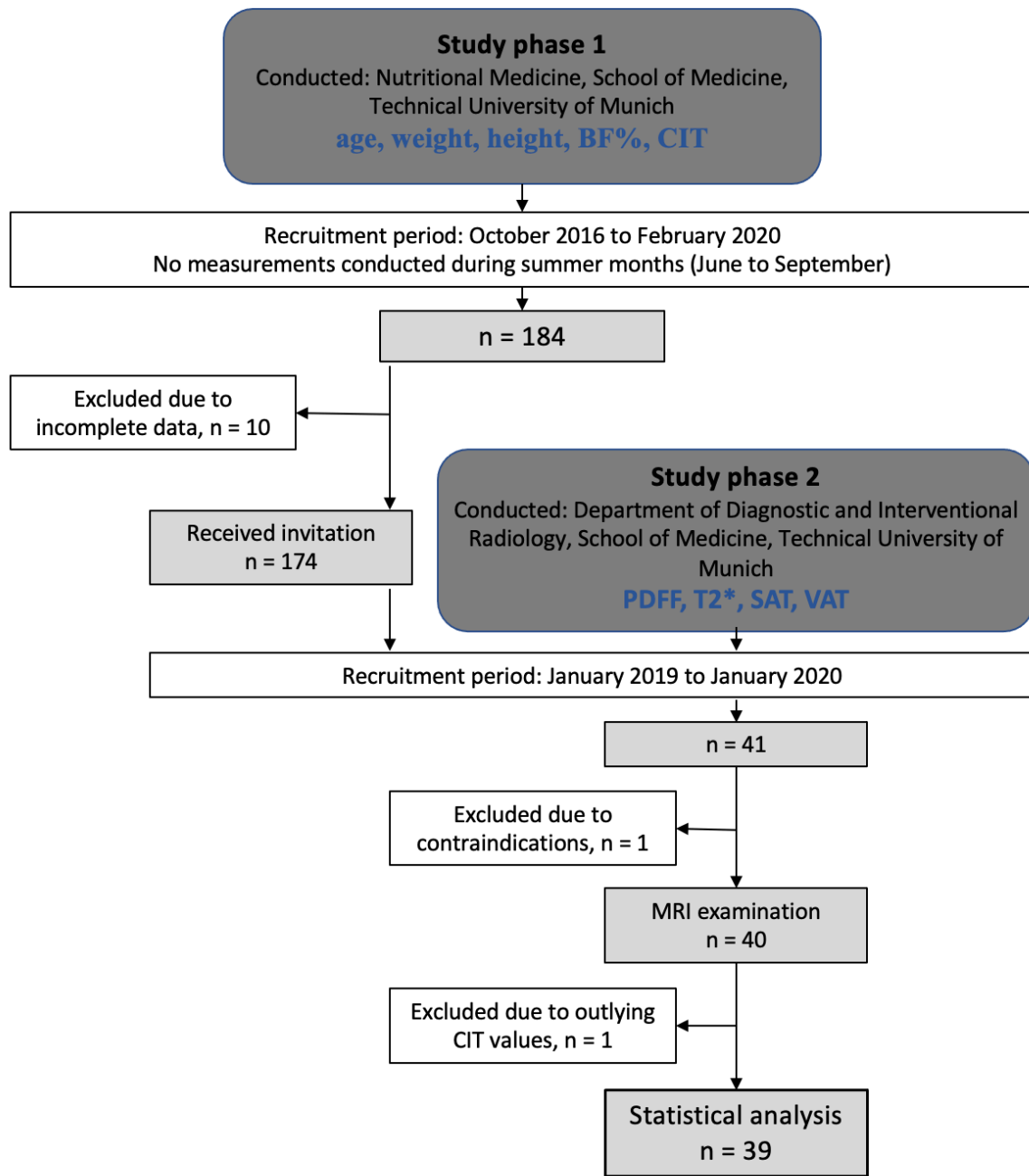
Figure 6: Flowchart of the study design, recruitment process and timing of acquired parameters. BF%, body fat percentage, BMI, body mass index; CIT, cold-induced thermogenesis, PDFF, proton density fat fraction, n, number, SAT, subcutaneous adipose tissue, T_2*, T_2-star, VAT, visceral adipose tissue.

5.2 Population

For the present analysis, the cohort of 40 participants with both available CIT and MRI data from first and second phase was analyzed closely. One volunteer was excluded due to significantly outlying CIT values in Grubbs Test. Hereafter a study population of 39 participants, 24 female and 15 male, was left for further statistical analysis.

5.3 Anthropometric measurements

On the first visit anthropometric examinations were conducted right in the morning between 6 a.m. and 8 a.m., on an empty stomach before CIT exploration. The body height was measured with a stadiometer (Seca, Hamubrg, Germany) and an accuracy down to the millimeter.

Body weight and body composition were assessed in one go, with the help of TANITA Body Composition Analyzer BC-418 MA (Tanita Europe GmbH, Sindelfingen, Germany) - a segmental body composition monitor based on BIA with an integrated body weight scale. According to manufacturer Tanita, BIA obtained an accuracy within ±5% compared to dual-energy absorptiometry (DEXA). The latter is a method based on x-ray diagnostics, which is currently besides whole-body MRI considered gold standard in body composition analysis.

BIA measurements were performed in minimal clothing, barefoot and after emptying the bladder. This, early morning timing and fasting status ensured uniform hydration levels, recommended by the manufacturer to achieve consistent readings.

5.3.1 Body mass index

From measured body weight in kg and height in m the BMI was calculated by applying the following formula. BMI is expressed in kg/m^2.

$$BMI = \frac{weight}{height^2}$$

5.3.2 Body fat percentage

Body fat mass expressed in kg resulting from BIA fat mass measurements and body weight allowed calculation of the body fat percentage (BF%) in %.

$$BF\% = \frac{fat\ mass}{body\ weight} \times 100$$

5.4 Cold-induced thermogenesis

To assess CIT under controlled conditions, participants had fasted for at least 10 hours, had not engaged in physical activity for at least 24 hours, and had to refrain from caffeine and alcohol. Subsequent to anthropometric exploration, REE was measured by indirect calorimetry; first at thermoneutrality and secondly under cold exposure by the use of individualized cooling protocols. For the examination, volunteers had to be at rest and laid between two water-perfused mattresses (Maxi-Therm Lite Blankets, Cincinnati Sub-Zero, OH, USA) connected to a temperature device (WiseCircu type WCR-P8, Witeg Labortechnik, Wertheim, Germany), allowing highly controlled temperature conditions.

5.4.1 Indirect calorimetry

The used Cosmed canopy system (COSMED Quark RMR, Fridolfing, Germany) allowed non-invasive measuring of O_2 consumption (VO_2) and CO_2 output (VCO_2) both measured in milliliter (ml) per minute (min). Each indirect calorimetry measurement, under thermoneutrality and under cold exposure, was performed for 30 min during which subjects reached steady state conditions, defined as a time span of at least 4 min in which deviation of VO_2 and VCO_2 were less than 10% [78]. A shortened Weir equation was used for calculation of REE from VO_2 and VCO_2[79] (compare 4.1.5.2).

5.4.2 Cooling protocol

The cooling protocol was described in a related publication before [80] and set up according to van der Lans et. al [81]. Firstly, REE was measured under thermoneutral conditions (REE_{TN}) and water temperature in the blankets was set to 32°C to set baseline. The afterwards applied cooling protocol was individualized, to ensure participants were kept above the individual shivering threshold. Therefore, water temperature was decreased stepwise as far as participants reported no shivering. When shivering was observed or reported by participants, water temperature was raised by 2°C until shivering stopped. This temperature was kept for a 120 min interval as cold exposure and afterwards REE under cold exposure (REE_{CE}) was measured for 30 min. In case shivering re-occurred in the 120 min interval, water temperature was raised again by two degrees and the 120 min were started again. If shivering occurred during the 30 min interval of measuring REE_{CE}, participants were excluded from the study.

5.4.3 Calculation of cold-induced thermogenesis

From the measured REE_{TN} and REE_{CE}, relative CIT in % was calculated as follows:

$$CIT = \frac{(REE_{CE} - REE_{TN})}{REE_{TN}} \times 100$$

5.5 MRI protocol

MRI examination was performed on a 3 Tesla system (Elition, Philips Healthcare, Best, Netherlands). The scanner room was air-conditioned and ensured stable ambient temperatures at 21°C. Before scanning, patients were given adequate time for acclimatization, while written informed consent was collected, and the procedure was explained in detail. Participants were placed in supine position, a sensor for respiratory monitoring was placed on the upper abdomen and fastened with a strap. Special attention was paid to proper alignment of the shoulders with neutral positioning according to neutral-zero-method. Cushioned pads and a triangular knee pad ensured comfortable positioning during the procedure. A finger pulse oximeter was placed on the left hand, to check that patients were in a relaxed state. A bell was given to volunteers in case of emergencies and an intercom system supported continuous patient contact, especially needed for special breathing commands. Total procedure time was around 45 min, dependent on individual breathing rate. During that time participants had to lay as still as possible and were asked to breathe calmly. The full scan protocol is shown in Table 3.

Table 3: Scan protocol including sequence, scan time and localization.

Sequence	Scan time	Localization
Survey	0:30 min	Neck, shoulders
12-echo mDixon	3:30 min	centered around clavicle bone
6-echo mDixon	2:30 min	
Survey		trunk
2-echo mDixon	0:30 min	from liver dome down to femoral head
2-echo mDixon	0:30 min	
12-echo mDixon	3 min	centered around L5 vertebra
6-echo mDixon	1 min	

Min, minute; L5 vertebra, 5th lumbar vertebra.

5.5.1   Supraclavicular and gluteal PDFF mapping

Both the neck and pelvic region were each scanned twice with multi-echo 3D-spoiled gradient echo sequences, firstly acquiring six echoes (6-echo mDixon) and secondly time-interleaved with six echoes and two acquisitions (12-echo mDixon). A small flip angle was used to reduce T_1 bias effects[82, 83].

Identification of the supraclavicular fat pocket was done on an MRI localizer sequence of the neck and centered around the clavicle bone. The investigator ensured inclusion of vocal cords and coracoid process to fully display the region defined as the supraclavicular adipose tissue depot. For the reduction of motion artifacts, a breathing trigger was applied, and data was only recorded in expiration phase with a zero-trigger delay.

The sequence for gluteal PDFF mapping was planned on the full body localizer and centered around L5 vertebra. Pelvic imaging was conducted in free breathing mode.

A complex-based water-fat separation algorithm of the manufacturer generated PDFF maps. The algorithm accounts for known confounding factors [84].

5.5.2   Imaging of adipose tissue volumes

For composition analysis two stacks of axial two-echo Dixon 3D-spoiled gradient echo (two-echo mDixon) images were acquired. For each stack one breath hold of 10.6 seconds was needed. In planning phase, the prior conducted full body localizer was used to ensure imaging of the whole trunk - from the upper liver dome down to the widest part of the femoral head.

5.6   Imaging data analysis

For the readout of quantitative MRI parameters, manual segmentation work was done using ITK-SNAP 3.8.0 (www.itksnap.org) [85] and regions of interest were defined by a combination of manual crude outlining, automatic processing, with subsequent manual control and correction. The exact procedure for each segmentation is explained in detail below. Automatic processing of the manual segmentation allowed quick alterations and combined with a customized python script (Python language version 2.7; Python Software Foundation, https://www.python.org/) enabled efficient readout of mean values.

5.6.1 Supraclavicular and gluteal segmentation

6-echo as well as 12-echo data was used for PDFF mapping. To ensure reproducibility for the supraclavicular and gluteal ROI, borders were predefined as follows.

Borders of the supraclavicular fat pocket were defined as:

1. In coronal plane:
    a. Cranial: vocal cords
    b. Caudal: undermost cut of the coracoid process
2. In axial plane:
    a. Anterior: rear edge of sternum
    b. Posterior: imaginary line from the acromioclavicular joint to the point of contact of M. levator scapulae and M. trapezius
    c. Lateral: imaginary line from the clavicle bone to acromioclavicular joint

Borders of the deep gluteal SAT were defined as:

1. In coronal plane:
    a. Cranial: top slice of L5 vertebra
    b. Caudal: undermost slice of L5 vertebra
2. In axial plane:
    a. Anterior: rear edge of iliac bone
    b. Posterior: deep body fascia

5.6.1.1 Processing steps performed to create final segmentation masks

Segmentation was performed on 6-echo data following the steps below:

1. Crude outlining of the ROI on every second slice (supraclavicular) or every slice (gluteal) in the axial plane was performed, while staying within the predefined borders.
2. Interpolation of the segmentation mask along the axial plain with help of ITK-SNAP to fill in the skipped slices was performed for supraclavicular data.
3. Automatic processing with a customized Python script which applied thresholds for PDFF and T_2^* values.
    a. A threshold of PDFF $\geq$ 50% was chosen for the exclusion of muscle, vessels, and lymph nodes, by simultaneously losing as little as possible data derived from BAT.

b. T_2* threshold was kept at 5 to 100 milliseconds (ms) to exclude bone.

4. In MATLAB (MathWorks, Natick, MA, USA) an additional erosion was performed to reduce partial volume effects on the edges of the segmentation mask.

5. Readout of mean values was performed by a customized Python script.

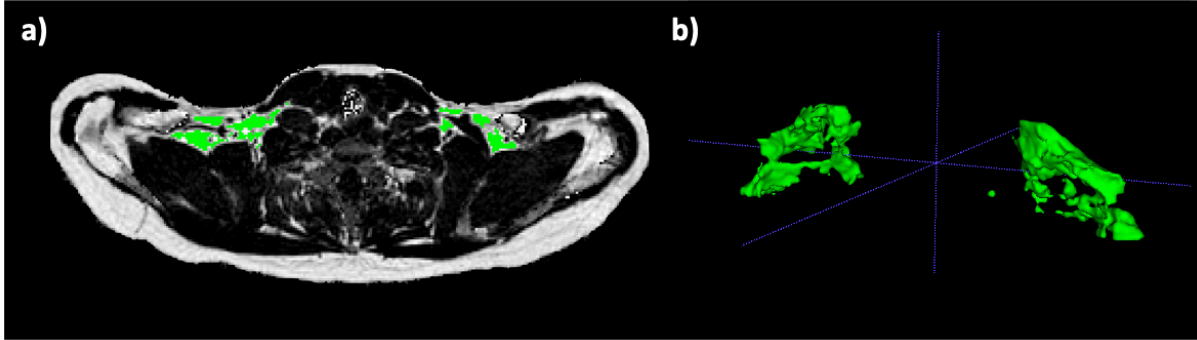An exemplary segmentation mask is shown in Figure 7.

Figure 7: Exemplary display of the bilateral segmentation mask of the supraclavicular fossa (green) after semiautomatic postprocessing. (a) PDFF map with bilateral segmentation mask in axial plane. (b) Three-dimensional reconstruction of bilateral segmentation mask presented from frontal oblique. PDFF, proton density fat fraction.

For the 12-echo data, segmentation masks, resulting from step 1 and 2, were resized according to different slice count and field of view, by a customized Python script. After resizing steps 3 to 5 were performed analogous to the processing of 6-echo data.

5.6.1.2 Supraclavicular and gluteal PDFF and T_2*

An automated readout of PDFF mean values was performed for the created masks of the supraclavicular and gluteal ROIs and supraclavicular PDFF ($PDFF_{SC}$), gluteal PDFF ($PDFF_{GLU}$) as well as supraclavicular T_2* (T_2*_{SC}) and gluteal T_2* (T_2*_{GLU}) were extracted.

For 12-echo data, $PDFF_{SC}$ and $PDFF_{GLU}$ mean values were extracted accordingly. Besides mean PDFF, 12-echo R_2* mean values were extracted and translated into T_2* values, according to the following formula.

$$T_2{}^* = \frac{1}{R_2{}^*}$$

A flowchart illustrating the process from segmentation, over thresholding, to finally read out of different mean values is found below in Figure 8. Please take note that earlier investigations rendered 6-echo data insufficient for T_2* analysis [66]. This is why 6-echo T_2* measures are solely used for segmentation and for comparison with 12-echo T_2* values, but not as quantitative BAT marker itself, whereas 12-echo T_2* is considered as possible indicator for BAT later on.
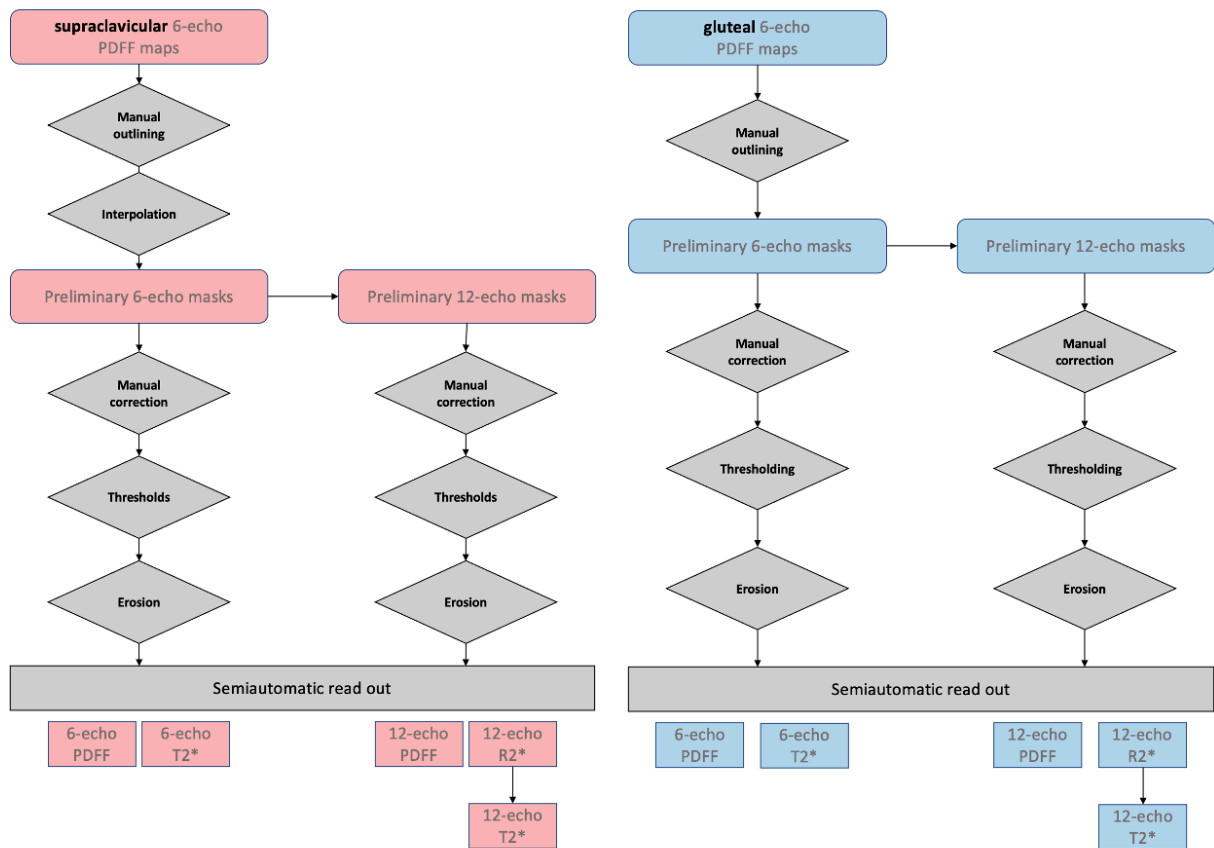

Figure 8: Flowchart illustrating data postprocessing. On the left supraclavicular data is displayed in red and on the right gluteal data displayed in blue. PDFF, proton density fat fraction, R_2, reciprocal value of T_2*, T_2*, T2-star.*

5.6.1.3 Calculation of Delta PDFF

The Delta PDFF ($PDFF_{DEL}$) was calculated as the difference of gluteal PDFF ($PDFF_{GLU}$) and supraclavicular PDFF ($PDFF_{SC}$).

$$PDFF_{DEL} = PDFF_{GLU} - PDFF_{SC}$$

5.6.1.4 Calculation of supraclavicular fossa volume

For the supraclavicular ROI, the volume was additionally assessed. Volume of the supraclavicular fossa (VOL_{SC}) is simply expressed as resulting voxel count for the final segmentation masks in 6- as well as 12-echo data.

5.6.2 Subcutaneous and visceral adipose tissue segmentation

Adipose tissue volumes SAT and VAT were assessed in a two-step semi-automatic process on two-echo Dixon data.

5.6.2.1 Semiautomatic segmentation of trunk

In the first step a Python-based tool pre marked SAT, VAT and remaining pixels as three different labels, which had to be corrected manually in a second step. Correction was performed manually in ITK-SNAP on each slice in axial plane. The upper border was represented by the liver dome and the lower border by the center of the femoral head, everything marked below or above in the automated first step was deleted manually in the second step. The approach was already used in several publications [64, 86] before.

5.6.2.2 Calculation of height adapted adipose tissue volumes

Since SAT and VAT are usually derived from whole body MRI, which was not available for this cohort, adipose tissue volumes were divided by trunk length, resulting in normalized values expressed in ml/cm. Trunk length from the liver dome to the femoral head was calculated from slice count and slice thickness. Normalized SAT and VAT volumes were calculated as follows:

$$SAT_{adapt} = \frac{SAT}{trunk\ length}$$

$$VAT_{adapt} = \frac{VAT}{trunk\ length}$$

For the sake of simplicity, adapted values SAT_{adapt} and VAT_{adapt} will be referred to as SAT and VAT in statistical analysis.

5.6.2.3 Calculation of MR-based trunk fat percentage

In addition, the fat proportion of the trunk – the trunk fat percentage (TF%) – was calculated, as an approximation for total body fat measurements conducted from whole body MRI, which again was not available. Hereby pixel count of adipose tissue volumes of the trunk, as well as the volume of all remaining non-fatty tissue (NFT) of the trunk were used for the calculation.

$$TF\% = \frac{SAT + VAT}{SAT + VAT + NFT}$$

MRI-based TF% is used for the validation of the BIA-based BF% under 6.2.

5.7 Statistical analysis

Statistics and plotting were performed with the help of IBM SPSS Statistics for MacOS version 26 (IBM Corp., Armonk, N.Y., USA). Variables were checked for normal distribution with the help of Shapiro-Wilk Test. Normally distributed parameters were weight, height, CIT, and BF% and are expressed in mean ± standard deviation (SD). All remaining values showed no normal distribution and will be expressed in median and range in parentheses.

Testing for difference was performed as non-parametric testing (Wilcoxon). Due to mainly not-normally distributed values, correlations were investigated with the help of Spearman's rank correlation coefficient (rho) and a two-tailed p-value of $p \leq 0.05$ was considered statistically significant. Moreover, the later partial correlation analysis was conducted as partial rank correlation to correctly examine the effect of influencing variables on the correlation of non-normally distributed values. Interobserver consistency for PDFF$_{SC}$ values was evaluated using the intraclass correlation coefficient.

5.7.1 Subgroup definition for correlation analysis

First the study cohort was divided into two subgroups based on BMI. BMI cutoffs, as defined by the WHO [87], were used to divide into a normal-weight subgroup (BMI < 25 kg/m²) and an overweight / obese subgroup (BMI ≥ 25 kg/m²). The shortcomings of BMI cutoffs especially in small and heterogenous cohorts are known, therefore, the cohort was grouped again, but via BF% cutoffs - more precise gender adapted cutoffs found in related literature [88-90]. This

resulted in a subgroup with normal BF% (male BF% ≤ 25% and female BF% ≤ 30%) and one with high BF% (male BF% > 25% and female BF% > 30%).

5.8 Visual analysis

All displayed MR-images were created in ITK-SNAP 3.8.0 (www.itksnap.org) [85]. Histograms for the conducted pixel by pixel analysis (5.8) were created in MATLAB (MathWorks, Natick, MA, USA).

5.8.1 Subgroup definition of BAT positive and BAT negative cohort.

For the purpose of visually analyzing the gathered MRI-data, two groups with likely BAT positive and likely BAT negative individuals were selected. This selection was performed by CIT cutoffs. Since CIT is known for interindividual variation the grouping was not performed via median CIT, but via quartiles. Therefore, the BAT negative cohort was represented by the first quartile and the BAT positive subgroup by the fourth quartile, representing the lowest 25% and highest 25% of data points.

6   Results

6.1   Characteristics of the study cohort

The study population of 39 participants, 24 female and 15 male, showed a median age of 27 years (20-53 years). Descriptive statistics for all parameters are summarized in Table 4.

Table 4: Descriptive statistics for all parameters sorted by normal / non-normal distribution.

Normally distributed	Mean ± SD (range)
Weight, kg	77.3 ± 17.1 (50.1 - 121.4)
Height, cm	174.3 ± 10.5 (157.2 -195.2)
BF%, %	25.2 ± 11.6 (4.6 - 45.3)
TF%, %	30.0 ± 11.7 (11.4 – 67.2)
CIT, %	4.7 ± 9.0 (-10.6 - 24.3)
6-echo: $T_2^*{}_{SC}$, ms	68.8 ± 10.1 (47.4 - 86.9)
12-echo: $T_2^*{}_{SC}$, ms	21.8 ± 4.7 (12.2 - 31.4)
12-echo: $T_2^*{}_{GLU}$, ms	41.7 ± 5.3 (28.5 - 51.0)
Not normally distributed	**Median (range)**
Age, years	27 (20 - 53)
BMI, kg/m^2	23.2 (19.0 - 38.5)
VAT, ml/cm	23.3 (4.0 - 184.2)
SAT, ml/cm	114.6 (28.6 - 447.9)
6-echo: $PDFF_{SC}$, %	82.5 (69.7 - 88.1)
6-echo: $PDFF_{GLU}$, %	91.1 (82.3 - 93.5)
6-echo: $PDFF_{DEL}$, %	8.8 (3.9 - 21.9)
6-echo: $T_2^*{}_{GLU}$, ms	71.8 (42.8 – 90.5)
6-echo: VOL_{SC}	12889 (2574 - 46084)
12-echo: $PDFF_{SC}$, %	84.1 (70.3 - 89.9)
12-echo: $PDFF_{GLU}$, %	93.3 (84.0 - 96.3)
12-echo: $PDFF_{DEL}$, %	8.3 (4.2 - 23.4)
12-echo: VOL_{SC}	5354 (1640 - 13377)

BF%, body fat percentage; BMI, body mass index; CIT, cold-induced thermogenesis; cm, centimeter; kg, kilogram; m, meter; ml, milliliter; ms, millisecond; $PDFF_{DEL}$, Delta proton density fat fraction; $PDFF_{GLU}$, Gluteal proton density fat fraction; $PDFF_{SC}$, Supraclavicular proton density fat fraction; SAT, subcutaneous adipose tissue; SD, standard deviation; $T_2^*{}_{GLU}$, Gluteal T_2^*; $T_2^*{}_{SC}$, Supraclavicular T_2^*; TF%, trunk fat percentage; VAT, visceral adipose tissue; VOL_{SC}, Volume of the supraclavicular fossa.

The cohort presented very heterogenous in terms of anthropometric measures. The median BMI was 23.2 kg/m^2, with a minimum of 19.0 kg/m^2 and a maximum 38.5 kg/m^2. Thus, according to WHO guidelines, the leanest participant was found on the lower end of normal weight,

whereas the heaviest participants were categorized as morbidly obese. This heterogeneity was also reflected in BF%, with a mean BF% of 25.2 ± 11.6% (4.6 - 45.3%). The calculated TF% showed similar, but slightly higher results, with a mean TF% of 30.0 ± 11.7 (11.4 – 67.2). Body adiposity depicted by MRI-measured adipose tissue volumes revealed widely dispersed adipose tissue volumes, with a median VAT of 23.3 ml/cm (4.0 – 184.2 ml/cm) and a median SAT of 114.6 ml/cm (28.6 – 447.9 ml/cm).

Assessment of the thermogenic potential resulted in a mean CIT of 4.7 ± 9.0 % (-10.6 – 24.3) in the whole study cohort. Please note occurring negative CIT results in some participants, which represent a decrease in REE under thermal challenges.

6.2 Validation of main descriptive marker for body adiposity

Primarily the BIA-based BF% was used as descriptive marker for body adiposity, but only after an extensive validation. BIA-based BF% was compared to the TF%, as a substitute for bodyfat percentage derived from full body MRI. Both measures, BF% and TF%, were designed to assess the same property and were evaluated for conformance with the help of the Bland-Altman method.

6.2.1 Correlation of TF% and BF%

Mean BF% was 25.2 ± 11.6 %, mean TF% was 30.0 ± 11.7% and the mean difference of both measures was 6.7 ± 6.8 %. Note the higher individual fat percentages measured by MRI compared to BIA. Correlation analysis of BF% and TF% revealed a strong correlation of both parameters (rho = 0.86, p < 0.001).

6.2.2 Agreement of TF% and BF%

For the Bland-Altman plot, the average of the two measures was plotted against the difference of the two measures and for easier interpretation lines were inserted for the mean of difference (full line) and for acceptable limits of agreement, as mean of difference ± 1.96 times standard deviation (dashed lines). The Bland-Altman plot is displayed in Figure 9.

The plot shows that the variance of deviation stays largely inside the accepted borders (limits of agreement), proving good agreement of both measures. However, scattering can be observed, pointing to a systemic deviation. This was quantified by statistical testing for difference.

Wilcoxon revealed a significant difference of both measures (p < 0.001), confirming the systemic error, with systemically higher TF% values. Based on these results, BIA-based BF% was used as main descriptive variable for body adiposity in the following.
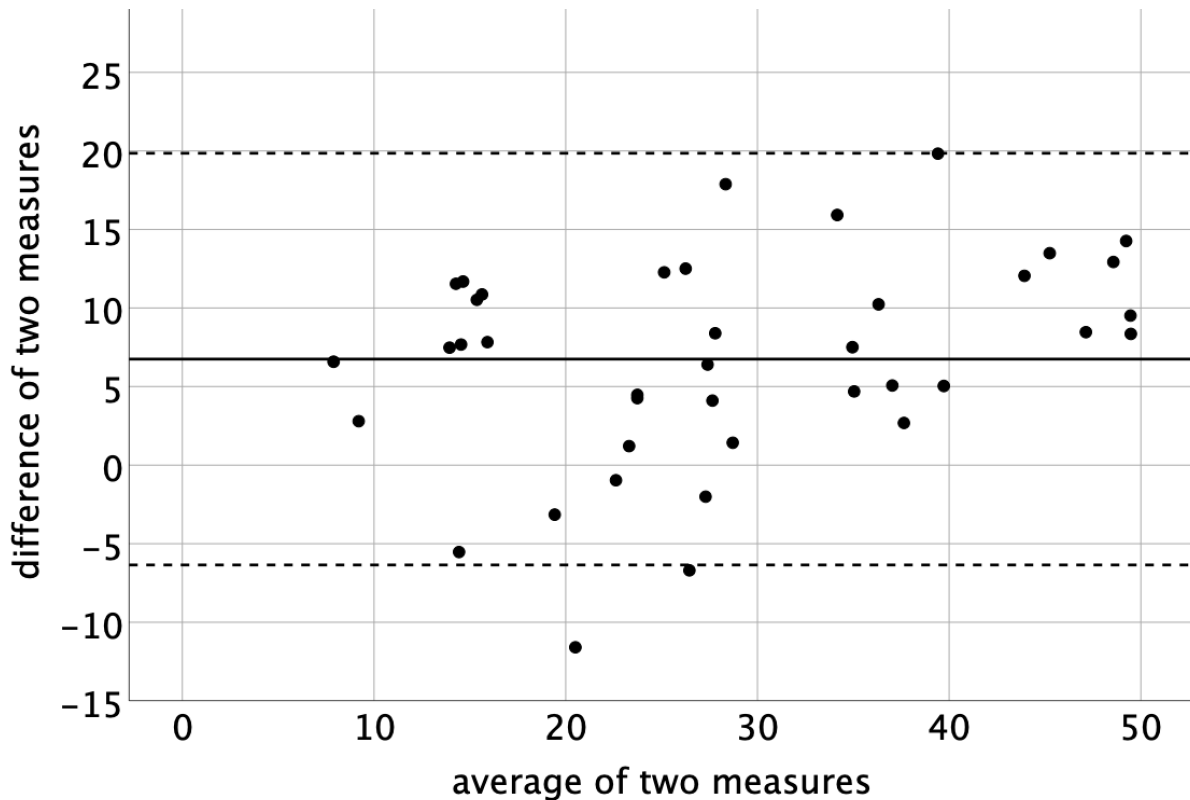

Figure 9: Bland-Altman Plot of MRI-based TF% and BIA-based BF%. Limits of agreement (dashed lines) and mean of difference (full line). BF%, body fat percentage; BIA, body impedance analysis; MRI, magnetic resonance imaging; TF%, fat percentage of trunk.

6.3 Validation of segmentation method

In this study the segmentation of the whole supraclavicular fat depot was performed largely automated, to minimize dependency of the single investigator and improve reproducibility. Therefore, the strictly stepwise performed segmentation, as explained in detail under 5.6, was checked for interobserver consistency in a sub cohort of five participants (12.8% of the study cohort).

Two fifth year medical students, with experience in whole body MRI, and one board certified radiologist performed manual segmentation in accordance with the predefined criteria (5.6.1). Those three raters achieved high agreement and reproducibility of $PDFF_{SC}$ values, with an interclass correlation coefficient of 0.97 (95% confidence interval, 0.73 to 1.0).

6.4 Comparison of 6-echo and 12-echo data

In 6-echo data, median $PDFF_{SC}$ was 82.5% (69.7 – 88.1%) and median $PDFF_{GLU}$ was 91.1% (82.3 – 93.5%). The readout of T_2^* results showed a mean $T_2^*_{SC}$ of 68.8 ± 10.1ms (47.4 - 86.9) and median $T_2^*_{GLU}$ of 71.8ms (42.8 – 90.5)

In 12-echo data, median $PDFF_{SC}$ was 84.1% (70.3 – 89.9%) and median $PDFF_{GLU}$ was 93.3% (84.0 – 96.3%). Over the supraclavicular ROI, a median supraclavicular R_2^* of 44.1Hz (33.7 – 81.7Hz) was found, thus median $T_2^*_{SC}$ of 22.7ms (12.2 – 28.7ms) was calculated. In the gluteal region, a median gluteal R_2^* of 24.0Hz (19.6 -35.1Hz) was measured, which resulted in calculated median $T_2^*_{GLU}$ values of 41.6ms (28.5 -51.0ms).

6-echo T_2^* results are only considered in comparison to 12-echo data and in the segmentation process. The supraclavicular and gluteal mean values of 6- and 12-echo data were contrasted visually with the help of boxplots in Figure 10.
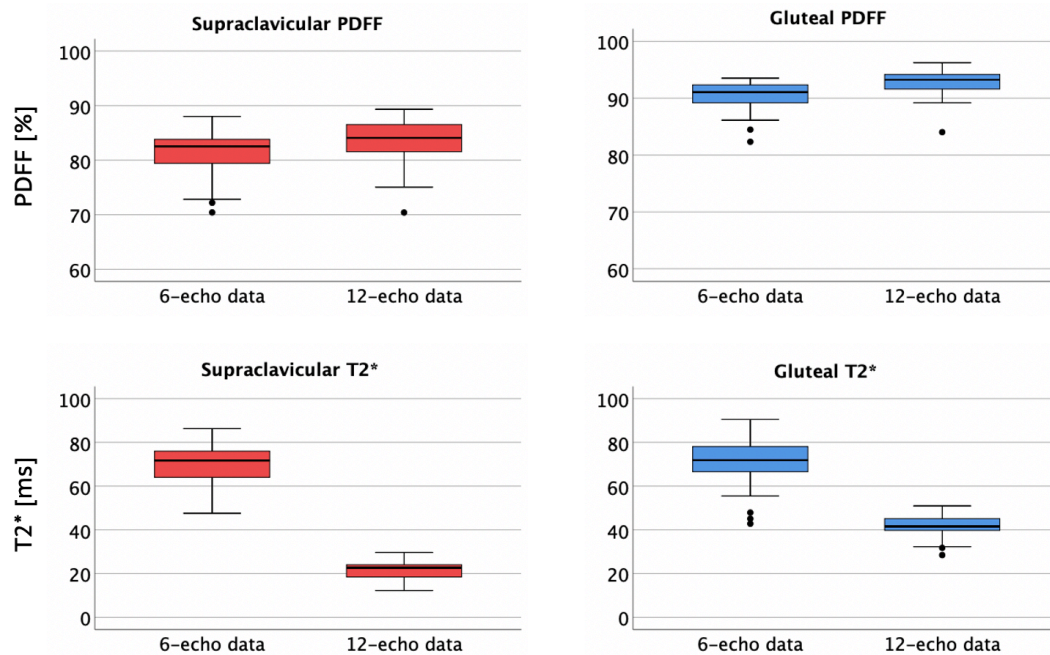
Figure 10: Comparison of supraclavicular and gluteal PDFF and T_2^* mapping in 6- and 12-echo data. Note the wider spreading of 6-echo T_2^* results in supraclavicular as well as gluteal measurements compared to 12-echo T_2^* results. ms, milliseconds; PDFF, Proton density fat fraction; T_2^*, T_2-star.

The observed differences were supported by non-parametric testing: $PDFF_{SC}$ and $PDFF_{GLU}$ of 6- and 12-echo data were significantly different, as well as $T_2^*_{SC}$ and $T_2^*_{GLU}$. All differences tested significant on a significance level of $p < 0.001$, as shown in Table 5.

Table 5: Comparison of 6- and 12-echo measurements and results of non-parametric testing.

	6-echo	12-echo	*6-echo vs 12-echo*
PDFF$_{SC}$ (%)	82.5 (69.7 - 88.1)	84.1 (70.3 - 89.9)	p < 0.001
PDFF$_{GLU}$ (%)	91.1 (82.3 - 93.5)	93.3 (84.0 - 96.3)	p < 0.001
PDFF$_{SC}$ vs PDFF$_{GLU}$	p < 0.001	p < 0.001	
T$_2$*$_{SC}$ (ms)	68.8 ±10.1 (47.4 - 86.9)	21.8 ±4.7 (12.2 – 31.4)	p < 0.001
T$_2$*$_{GLU}$ (ms)	71.8 (42.8 - 90.5)	41.7 ±5.3 (28.5 - 51.0)	p < 0.001
T$_2$ $_{SC}$ vs T$_2$*$_{GLU}$*	p < 0.001	p < 0.001	

ms, millisecond; PDFF$_{GLU}$, gluteal proton density fat fraction, PDFF$_{SC}$, supraclavicular proton density fat fraction, T$_2$*$_{GLU}$, gluteal T$_2$*; T$_2$*$_{SC}$ supraclavicular T$_2$*, vs, versus.

6.5 The difference of supraclavicular and gluteal PDFF

In 6- and 12-echo data, a significant difference of PDFF$_{SC}$ and PDFF$_{GLU}$ (p < 0.001) was detected (Table 5), with lower PDFF results for the supraclavicular compared to the gluteal ROI. This difference is exemplary visualized in Figure 11.
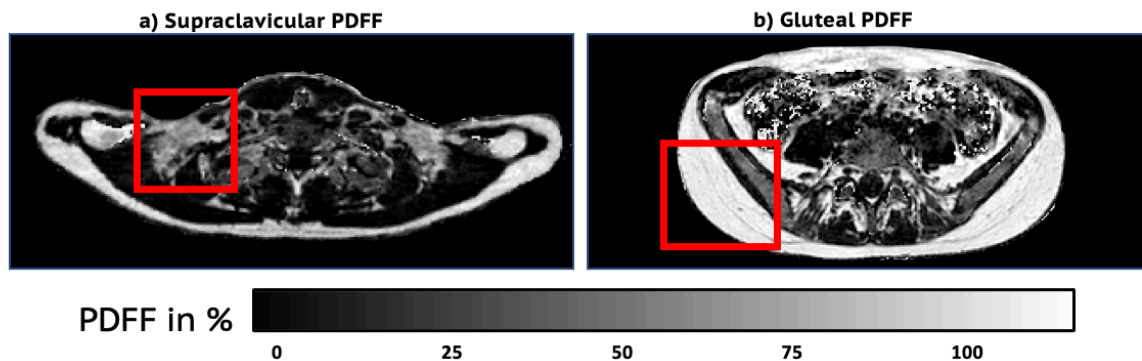
Figure 11: Comparison of 6-echo PDFF maps of the supraclavicular fat depot, as typical BAT region (a), and the subcutaneous gluteal WAT depot (b) in the same participant: A female 20-year-old with a BMI of 20.2 kg/m^2 and a CIT of 18,0%. Mean PDFF values over the investigated segmentation masks were a PDFF$_{SC}$ of 69,7% and a PDFF$_{GLU}$ of 91.5%. Both regions of interest are marked with a red box respectively. Note, the red box simply marks the ROI, but does not depict the 3D segmentation masks used for PDFF mean value read out. BAT, brown adipose tissue; BMI, body mass index; CIT, cold-induced thermogenesis; PDFF, proton density fat fraction; PDFF$_{GLU}$, gluteal proton density fat fraction, PDFF$_{SC}$, supraclavicular proton density fat fraction; ROI, region of interest, WAT, white adipose tissue.

The intraindividual difference of both ROIs was expressed in the calculated parameter PDFF$_{DEL}$. Median PDFF$_{DEL}$ in 6-echo data was 8.8% (3.9 - 21.9) and in 12-echo data 8.3% (4.2 - 23.4). In contrast to the results above (6.4), no significant difference for PDFF$_{DEL}$ of 6- and 12-echo data was detected (p = 0.435).

6.6 MRI parameters in relation to markers of obesity

Supraclavicular and gluteal MRI parameters were examined in their relation to markers of obesity; precisely to the anthropometric parameters BMI and BIA-based BF%, as well as to the MRI-measured adipose tissue volumes SAT and VAT.

6.6.1 PDFF correlates to BMI, BF% and adipose tissue volumes

In 6- as well as 12-echo data, $PDFF_{SC}$ correlated significantly to both markers of obesity, BMI and BF%, as well as 12-echo $PDFF_{GLU}$. Whereas 6-echo $PDFF_{GLU}$ only showed significant correlation to BF%, but not to BMI. For both datasets, measured $PDFF_{SC}$ and $PDFF_{GLU}$ correlated significantly to VAT and SAT ($p < 0.001$).

The calculated parameter $PDFF_{DEL}$ showed no significant correlation to both obesity markers in 6- and 12-echo data. Apart from a significant correlation of 12-echo $PDFF_{DEL}$ to VAT, no significant correlations to measured adipose tissue volumes was found for $PDFF_{DEL}$. Table 6 gives an overview of all correlation results concerning PDFF measurements to the descriptive parameters of obesity.

Table 6: Correlations of parameters of obesity to PDFF measurements, in 6a) for 6-echo data and in 6b) for 12-echo data.

6a)	BMI	BF%	SAT	VAT
6-echo $PDFF_{SC}$	rho = 0.39, p = 0.014	rho = 0.37, p = 0.019	rho = 0.55, p <0.001	rho = 0.59, p <0.001
6-echo $PDFF_{GLU}$	rho = 0.30, p = 0.067	rho = 0.49, p = 0.002	rho = 0.64, p <0.001	rho = 0.55, p <0.001
6-echo $PDFF_{DEL}$	rho = -0.26, p = 0.114	rho = -0.003, p = 0.985	rho = -0.08, p = 0.649	rho = -0.26, p = 0.108

6b)	BMI	BF%	SAT	VAT
12-echo $PDFF_{SC}$	rho = 0.35, p = 0.031	rho = 0.41, p = 0.01	rho = 0.53, p = 0.001	rho = 0.55, p <0.001
12-echo $PDFF_{GLU}$	rho = 0.32, p = 0,048	rho = 0.49, p = 0.002	rho = 0.66, p <0.001	rho = 0.57, p <0.001
12-echo $PDFF_{DEL}$	rho = 0.32, p = 0.045	rho = -0.22, p = 0.174	rho = -0.25, p = 0.123	rho = -0.36, p = 0.025

BF%, body fat percentage; BMI, body mass index; CIT, cold-induced thermogenesis; $PDFF_{DEL}$, Delta proton density fat fraction; $PDFF_{GLU}$, Gluteal proton density fat fraction; $PDFF_{SC}$, Supraclavicular proton density fat fraction; SAT, subcutaneous adipose tissue; VAT, visceral adipose tissue.

Further the assessed volume of the supraclavicular segmentation mask (VOL_{SC}) for 6- and 12-echo data was investigated. VOL_{SC} correlated significantly to BMI, BF% and all measured PDFF parameters in 6- and 12-echo data (Table 7).

Table 7: Correlations for supraclavicular volume (VOL_{SC}) to anthropometric parameters of obesity and PDFF measurements, in 7a) for 6-echo data and in 7b) for 12-echo data.

7a)	BMI	BF%	6-echo PDFF$_{SC}$	6-echo PDFF$_{GLU}$	6-echo PDFF$_{DEL}$
6-echo VOL$_{SC}$	rho = 0.62, p <0.001	rho = 0.50, p = 0.001	rho = 0.79, p < 0.001	rho = 0.63, p < 0.001	rho = -0.39, p = 0.014

7b)	BMI	BF%	12-echo PDFF$_{SC}$	12-echo PDFF$_{GLU}$	12-echo PDFF$_{DEL}$
12-echo VOL$_{SC}$	rho = 0.41, p = 0.009	rho = 0.39, p = 0.015	rho = 0.74, p < 0.001	rho = 0.39, p = 0.014	rho = -0.66, p < 0.001

BF%, body fat percentage; BMI, body mass index; CIT, cold-induced thermogenesis; PDFF$_{DEL}$, Delta proton density fat fraction; PDFF$_{GLU}$, Gluteal proton density fat fraction; PDFF$_{SC}$, Supraclavicular proton density fat fraction; VOL$_{SC}$, volume of supraclavicular fossa

6.7 Correlation of supraclavicular PDFF to CIT in 6-echo data

No significant correlation of PDFF$_{SC}$ and CIT was detected (rho = -0.154, p = 0.350) for the whole cohort. Exemplary, the PDFF maps of an individual with high CIT and an individual with low CIT can be compared in Figure 12.
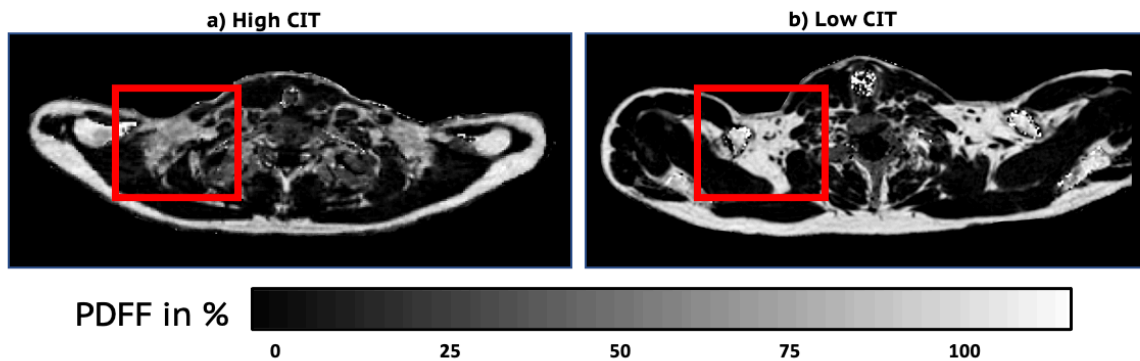
Figure 12: Exemplary display of difference in PDFF values in the supraclavicular fat depot of an individual (a) with high CIT results (CIT: 18.0%, PDFF$_{SC}$: 69.7%) compared to an individual (b) with low CIT results (CIT: 2.0%, %, PDFF$_{SC}$:84.8%). The high CIT participant was female, 20 years old with a BMI of 20,2kg/m². The low CIT participant was male, 26 years old with a BMI of 22.8kg/m². Both ROIs are marked with red box respectively. Note, the red box simply marks the ROI, but does not depict the 3D segmentation masks used for PDFF mean value read out. BMI, body mass index; CIT, cold-induced thermogenesis; PDFF, proton density fat fraction; PDFF$_{SC}$, supraclavicular proton density fat fraction; ROI, region of interest.

6.7.1 Correlation of PDFF and CIT in the whole group and subgroups by BMI and BF%

No significant correlation of $PDFF_{SC}$ and CIT was detected (rho = -0.154, p = 0.350) for the whole cohort. Both BMI subgroups showed no significant correlation of $PDFF_{SC}$ and CIT, but in the normal weight subgroup the inverse correlation improved (rho = -0.292 and p = 0.157), compared to the whole cohort. The high BF% subgroup showed no significant relation of $PDFF_{SC}$ and CIT, but in the normal BF% subgroup a significant correlation of $PDFF_{SC}$ and CIT was detected (rho = -0.530, p = 0.008). Results of correlation analysis of $PDFF_{SC}$ and CIT of the 6-echo dataset, including subgroups, are shown in Table 8.

Table 8: Results of correlation analysis of $PDFF_{SC}$ to CIT.

Subgroups	N	Correlation of $PDFF_{SC}$ to CIT
Whole cohort	39	rho = -0.154, p = 0.350
Normal weight (BMI <25 kg/m²)	25	rho = -0.292, p = 0.157
Overweight/obese (BMI ≥25 kg/m²)	14	rho = 0.218, p = 0.455
Normal BF% (male BF% <25%, female BF% <30%)	24	**rho = -0.530, p = 0.008**
High BF% (male BF% ≥25%, female BF% ≥30%)	15	rho = 0.250, p = 0.369

BF%, body fat percentage; BMI, body mass index; CIT, cold-induced thermogenesis; $PDFF_{SC}$, Supraclavicular proton density fat fraction. Note, significant results highlighted in bold.

6.7.2 Referencing to gluteal PDFF

Those results further indicated body adiposity as a confounding factor for PDFF measurements and the approach of referencing to $PDFF_{GLU}$ was pursued in the following. A conducted partial rank correlation for $PDFF_{SC}$ to CIT, corrected for $PDFF_{GLU}$, returned significant results in the whole cohort (rho = -0.32, p = 0.05). $PDFF_{DEL}$ in relation to CIT was examined in the whole cohort and the correlation of $PDFF_{DEL}$ and CIT was significant (rho = 0.37, p = 0.02).

6.8 Correlation of supraclavicular PDFF and T_2^* to CIT in 12-echo data

The investigation of 12-echo MRI-measurements in relation to CIT was executed analogous to the 6-echo analysis, with the additional investigation of T_2^*. No significant correlation of supraclavicular MRI-measurements to CIT was observed, neither for $PDFF_{SC}$ to CIT (rho = -0.125, p = 0.447), nor for $T_2^*_{SC}$ to CIT (rho = -0.068, p = 0.680).

6.8.1 Correlation of PDFF and T_2^* to CIT for subgroups by BMI and BF%

Similar as in 6-echo data, no significant correlation was found for $PDFF_{SC}$ to CIT, neither in the normal weight subgroup nor in the overweight subgroup. For the normal weight subgroup correlation was expectantly inverse (rho = -0.365, p = 0.072) and stronger compared to 6-echo results (rho = -0.29 and p = 0.16). Moreover, with the additional information about T_2^*, a significant inverse correlation of $T_2^*_{SC}$ to CIT was detected in the normal weight subgroup (rho = -0.405, p = 0.045), but not in the overweight subgroup (rho = 0.235, p = 0.418).

In the cohort with normal BF%, a strong significant correlation of $PDFF_{SC}$ to CIT (rho = -0.68, p < 0.0001), as well as for $T_2^*_{SC}$ to CIT (rho = 0.669, p < 0.0001) was observed. When checking the high BF% subgroup, no significant correlation for $PDFF_{SC}$ and CIT was detected, but for $T_2^*_{SC}$ to CIT a significant correlation was found (rho = 0.518, p = 0.048). In contrast to prior results in the normal BF% subgroup, this relation showed a positive correlation. Results of correlation analysis of supraclavicular MRI measurements (PDFF, T_2^*) to CIT for the whole cohort and broken down by subgroups are shown in Table 9.

Table 9: Results of correlation analysis of supraclavicular MRI measurements to CIT.

Subgroups	N	Correlation of $PDFF_{SC}$ to CIT	Correlation of $T_2^*_{SC}$ to CIT
Whole cohort	39	rho = - 0.125, p = 0.447	rho = -0.068, p = 0.680
Normal weight (BMI <25 kg/m²)	25	rho = -0.365, p = 0.072	**rho = -0.405, p = 0.045**
Overweight/obese (BMI ≥25 kg/m²)	14	rho = 0.187, p = 0.523	rho = 0.275, p = 0.342
Normal BF% (male BF% <25%, female BF% <30%)	24	**rho = -0.680, p < 0.001**	**rho = -0.669, p < 0.001**
High BF% (male BF% ≥25%, female BF% ≥30%)	15	rho = 0.389, p = 0.152	**rho = 0.518, p = 0.048**

BF%, body fat percentage; BMI, body mass index; CIT, cold-induced thermogenesis; cm, centimeter; kg, kilogram; m, meter; N, number; $PDFF_{SC}$, Supraclavicular proton density fat fraction; $T_2^*_{SC}$, supraclavicular T_2^*. Note, significant results highlighted in bold.

The relation of the supraclavicular MRI measurements $PDFF_{SC}$ and $T_2^*_{SC}$ to CIT is displayed in the scatterplots divided by subgroups, based on BMI as well as on BF% (Figure 13). Note in

Figure 13b and 13d how individuals with high CIT and simultaneously high BF% values dilute the inverse relation of CIT and PDFF$_{SC}$ and T$_2$*$_{SC}$ respectively.
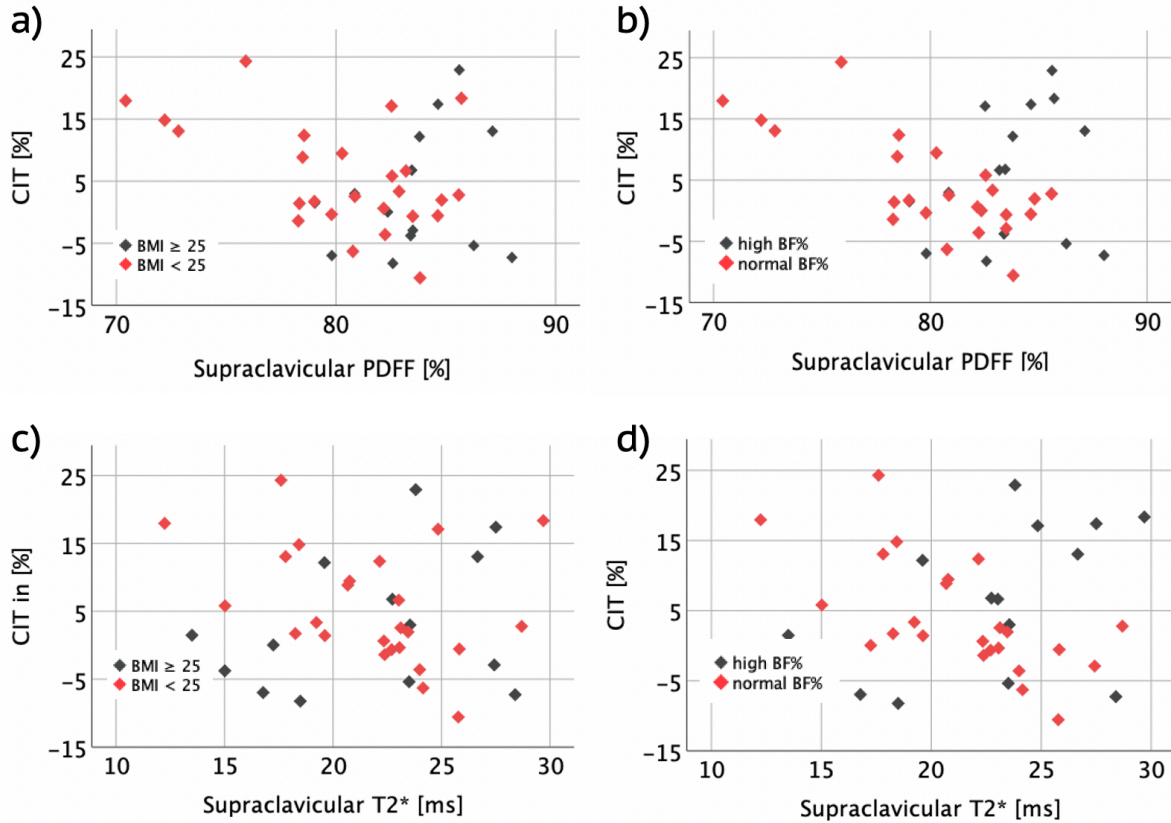
Figure 13: Scatterplots of supraclavicular PDFF (top row, a,b) and T$_2$ (bottom row,c,d) measurements in relation to CIT with all four subgroups displayed in different color. Left (a,c): Displayed subgroups by BMI (normal-weight subgroup, BMI < 25 and overweight / obese subgroup, BMI ≥ 25). Right (b,d): Displayed subgroups by BF% (normal BF%; male BF% ≤ 25% and female BF% ≤ 30% and high BF%; male BF% > 25% and female BF% > 30%). Please note individuals displaying high CIT and high BF% values at the same time. BF%, body fat percentage; BMI, body mass index; CIT, cold-induced thermogenesis; PDFF, proton density fat fraction; T$_2$*, T$_2$-star.*

6.8.2 Referencing to gluteal PDFF

In contrast to 6-echo results, no significant correlation of PDFF$_{DEL}$ and CIT was detected (rho = 0.278, p = 0.087). Equally partial rank correlation of PDFF$_{SC}$ and CIT controlled by the confounding variable PDFF$_{GLU}$, returned only borderline significant results (rho = -0.319, p = 0.051).

6.9 Pixel by Pixel analysis in 12-echo data

As under 5.8.1 explained, cohorts of nine individuals with likely BAT negative and likely BAT positive individuals were formed. Selected BAT negative participants showed CIT < -1.4 % and BAT positive ones showed CIT > 12.4 %. The BAT negative subgroup had a median age of 29 years, a median BMI of 27.3 kg/m^2, and a median BF% of 29.5 %. The BAT positive cohort had a median age of 28 years, while median BMI was 22.8 kg/m^2, and median BF% was 31.2 %. Since body adiposity was found to be a pivotal confounder in the prior analysis, both subgroups were tested for difference with the help of Mann-Whitney U test, regarding BMI and BF%. No significant difference between the two subgroups was found, neither for BMI (p = 0.161) nor for BF% (p = 0.931). Characteristics of both subgroups are displayed in Table 10.

Table 10: Characteristics of BAT negative and BAT positive cohorts and results of non-parametric testing.

	BAT negative	**BAT positive**	**BAT positive vs. BAT negative**
(N)	9	9	
Female (%)	5 (56)	7 (78)	
Normally distributed	*Mean ± SD (range)*	*Mean ± SD (range)*	*p-value*
BF%, %	27.4 ± 11.4 (10.2 - 42.9)	27.4 ± 12.4 (7.8 - 42.1)	p = 0.931
CIT, %	-6.1 ± 2.5 (-10.6 - -2.9)	17.7 ± 3.9 (13.0 - 24.3)	p < 0.0001
Not normally distributed	*Median (range)*	*Median (range)*	*p-value*
Age, years	29 (24-51)	28 (20 - 37)	p = 0.546
BMI, kg/m^2	27.3 (19.8 -36.3)	22.8 (19.0 - 34.1)	p = 0.161
PDFF$_{SC}$, %	85.0 (82.6 -89.0)	86.6 (70.4 - 89.3)	p = 0.931

BAT, brown adipose tissue; BF%, body fat percentage; BMI, body mass index; CIT, cold-induced thermogenesis; PDFF$_{SC}$, Supraclavicular proton density fat fraction.

6.9.1 PDFF histogram analysis

Histograms of the BAT negative and positive cohort are shown in Figure 14. The expected shift / peak towards lower PDFF percentages in the BAT positive cohort was not observed, or rather exclusively in lean individuals (14.2 a-d). Histograms found to be mainly driven by adiposity and therefore were sorted by ascending BF%, from left to right and top to bottom for better visualization.

14.1 BAT negative
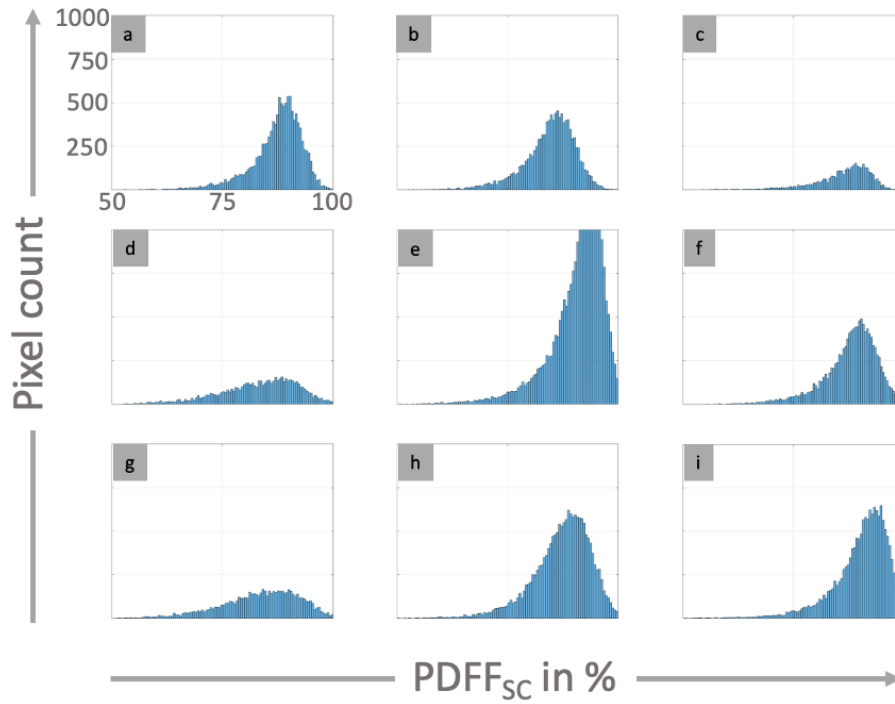
14.2 BAT positive
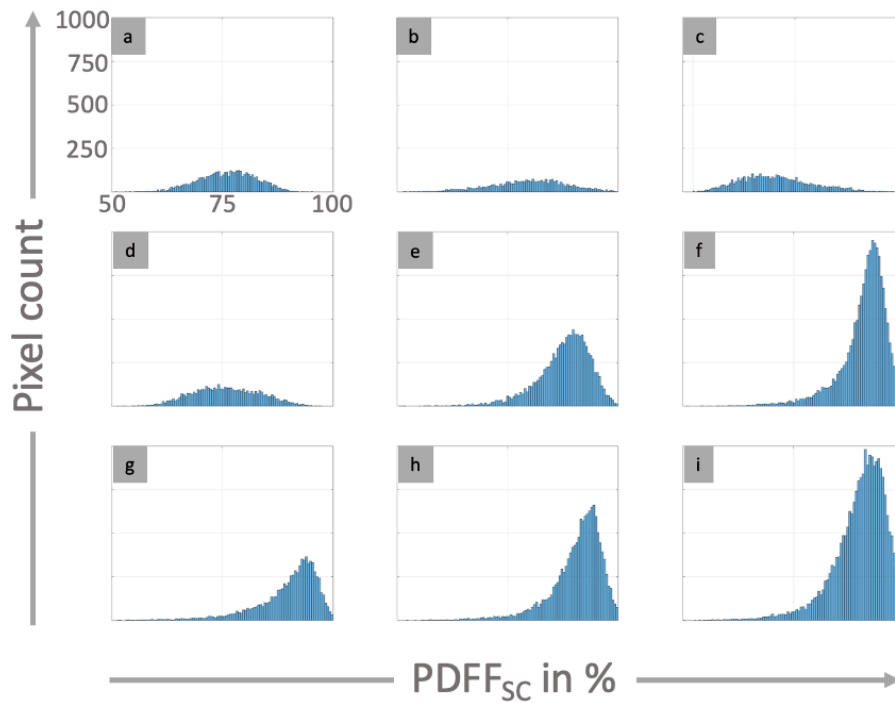
Figure 14: Histograms of supraclavicular PDFF for the BAT negative (14.1) and the BAT positive (14.2) cohort. Each y-axis displays pixel count from 0 to 1000 and each x-axis displays PDFF values from 50 to 100%, as examplary shown in the first histogms of 14.1 and 14.2. Histograms of each cohort are sorted by ascending BF% from left to right and from top to bottom. The BF% values for 14.1 are: a) 10.2%, b) 12.0%, c) 21.0%, d) 26.2%, e) 29.5%, f) 29.8%, g) 37.2%, h) 37.9%, i) 42.9% and for 14.2 are: a) 7.8%, b) 10.2, c) 21.6%, d) 26.3%, e) 31.2%, f) 31.2%, g) 34.5%, h) 42.1%, i) 42.1%. BAT, brown adipose tissue; BF%, body fat percentage; PDFF$_{SC}$, supraclavicular proton density fat fraction. .

7 Discussion

Evaluating the association between PDFF$_{SC}$ and CIT was the main goal of the present investigation. CIT represents an indirect functional parameter for BAT, while PDFF characterizes its morphology. The aim of this study was to establish a quick and easy tool for BAT characterization via MRI at ambient temperature and thus assessing an individual's capacity for calorie combustion in BAT without the need of prior activation.

7.1 Ensuring methodical correctness

Supraclavicular fat fractions reported in the literature show great variation [91]. Partly this is based on different activation stages of the examined BAT organ. Some studies report fat fractions under thermal challenges and usually values pre- and post-cold exposure [57-60, 63, 65], while other studies report values under ambient temperature [56, 62, 92-95]. Additionally, the structure of human BAT, with a mixture of brown and white adipocytes embedded in complex anatomy, complicates uniform and equivalent segmentation, worsening the influence of partial volume effects. When evaluating mean values derived from quantitative MRI, the applied segmentation method and the selected ROI are decisive for the outcome. Therefore, in this study immense efforts were made to implement a robust, reproducible, and comparable segmentation method upfront: Clear criteria for the segmentation were developed, partial volume effects were minimized (threshold, erosion) and the whole process was performed semiautomatically to reduce the dependence on the individual examiner. The results regarding interrater reliability showed excellent agreement and reproducibility, demonstrating that it is possible to minimize methodical faults beforehand and produce comparable and in particular reproducible data.

Adipose tissue PDFF in itself, both in potentially BAT-containing areas and in pure WAT, is highly dependent on the individual nutritional status and shows strong correlations to BMI and other anthropometric markers of obesity [64]. Hence, the presently reported mostly significant correlations of PDFF$_{SC}$ and PDFF$_{GLU}$ to all MR adipose tissue volumes, as well as to the anthropometric markers BMI and BF%, are in line with previous publications [64]. Other studies found relations of anthropometric measurements to MRI fat fraction and depicted the dependence to BMI and overweight [65, 93, 95]. Moreover, this association was also found under different thermal conditions and across all weight groups [65]. Those findings suggest overweight as possible confounding factor.

As the present cohort showed a wide range of weight (50.1 – 121.4 kg) and BMI (19.0 – 38.5 kg/m^2), it became apparent that body adiposity had to be considered for further evaluation. However, different exploration techniques for body composition (4.3 Measuring body adiposity) are vigorously discussed in the corresponding literature. For example, BMI is a good parameter for obesity classification on a population scale basis [23], even though the individual diagnostic performance for obesity by commonly used BMI cutoffs is poor. Thus, BMI as individual marker for body fat mass is increasingly criticized: A meta-analysis of 32 research studies from 12 countries, performed to clarify the diagnostic performance of BMI [68], resulted in a good specificity, but poor sensitivity. With a sensitivity around 50%, half of the individuals labeled as not obese showed abnormal adiposity, compared to body composition techniques measuring BF%. A limited diagnostic accuracy was also found by a similar cross-sectional study [69], with more than 10.000 individuals, comparing the diagnostic performance of BMI to BF% measured by BIA. BIA has the potential to provide remedy, if proper use (e.g., tetra polar device, fitting equations) is ensured [71, 72]. Whole-body MRI is one of the strongest tools to evaluate body composition [76], but no whole-body MR-data was available in the present study, therefore BIA-based BF% values were validated by MR-based TF%. A similar approach was found in a study, evaluating body fat distribution as risk factor for cerebrovascular disease [96]. The observed systemic deviation, with systematically higher TF% than BF% values, can be explained by lacking inclusion of the extremities in the MR-based method. However, the strong correlation and high agreement of both measures indicated high data quality and reliability of BIA-based BF% and justified its use as main descriptive value for body adiposity in this statistical analysis.

7.2   The association of supraclavicular MRI measurements and CIT

The main hypothesis is based upon the difference of BAT and WAT not only in function, but also in morphology and cellular composition. This leads to possible BAT detection via MRI without the need of activation, cold acclimatization, or ionizing radiation. The present results show a significant difference in PDFF$_{SC}$ and PDFF$_{GLU}$ in 6- as well as 12-echo data and are in line with many studies in the field [56, 60, 62, 64, 93, 95, 97]. Those studies report a difference in PDFF or fat fraction over the supraclavicular fat depot, compared to fat depots typically dominated by white adipocytes and represent the MRI correlate of different tissue composition, histological morphology, and supposedly the predominance of either BAT or WAT. The

approach of BAT detection in this study is based on the differentiation of BAT and WAT depots in a metabolically inactive state and was applied several times before [57, 58, 62].

The expected association of $PDFF_{SC}$ to CIT could neither be found in 6- nor in 12-echo data. This corresponds to other studies reporting on supraclavicular fat fraction [98] and PDFF [99] in relation to the assessed individual thermogenic potential under cold exposure. Please note that Gashi et al. excluded individuals with BMI > 30, hereby actually excluding individuals of special interest due to high interventional potential and Sun et al. only corrected for body weight in kg. In both studies no precise evaluation of body adiposity as possible confounder was performed, possibly disguising an existing relation in a similar manner as in the present data.

For this purpose, the association between $PDFF_{SC}$ and CIT was investigated, with the aid of subgroups based on BMI and BF% cutoffs. The correlation between $PDFF_{SC}$ to CIT strengthened in the BMI-based normal-weight subgroup, becoming significant in 6-echo data and borderline significant in 12-echo data. The corresponding overweight subgroup returned no significant correlation at all. When grouping was performed according to BF% cutoffs the correlation became significant for both datasets. This demonstrates an existing relation of supraclavicular fat fraction to individual thermogenic potential, at least in individuals with low or normal body fat mass. Seemingly this association is weakened with increasing body adiposity, possibly due to the omnipresent and dominant white adipocytes in individuals with higher body fat mass. The results for BMI- and BF%-based subgroups support the claim that BMI is lacking informative value for an individual's adiposity or rather body fat mass [68].

The partial rank correlation controlled by $PDFF_{GLU}$ for the whole cohort indicated that an inverse relationship of $PDFF_{SC}$ and CIT exists not only in lean but also in overweight individuals exhibiting high BF% values. However, this relation is weakened with growing BF%, rendering BAT detection by MRI in heterogenous cohorts hard to accomplish.

The novel marker $PDFF_{DEL}$ was developed based upon the above findings and depicts the individual difference of $PDFF_{GLU}$ and $PDFF_{SC}$. This method of intraindividual referencing to WAT-PDFF accounts for body adiposity and consequently $PDFF_{DEL}$ correlated significantly with CIT in the whole cohort in 6-echo data and borderline significantly in 12-echo data. Apparently, a high individual difference between the two adipose tissue depots indicates high CIT measurements, thus high $PDFF_{DEL}$ values could mean an increased likelihood of BAT presence in the supraclavicular fossa and eventually an increased thermogenic potential. This is supported by other studies in the field reporting brown adipocytes contributing to REE [8, 100, 101] or at least contributing to non-shivering thermogenesis post cold exposure [12, 29].

Interestingly the beforehand explored relation of PDFF measurements to body adiposity returned mostly strong and significant correlations with two exceptions: BMI, likely due to its poor informative value, and PDFF$_{DEL}$. PDFF$_{DEL}$ did not correlate with BF% or SAT and VAT volumes in 6-echo data and only with VAT in 12-echo data, emphasizing its independence from body adiposity. Admittedly when VOL$_{SC}$ was assessed, significant correlations were found with BMI, BF%, PDFF$_{GLU}$, PDFF$_{SC}$ as well as PDFF$_{DEL}$, indicating that the confounding effect of increasing bodyfat mass on PDFF parameters is weakened, but not fully resolved for the marker PDFF$_{DEL}$.

The concealment of potentially present brown adipocytes, by the sheer dominance of white adipocytes in participants with higher BF%, was also apparent in the presented histogram analysis, performed for 12-echo data. The BAT positive and BAT negative groups differed solely in CIT values and showed no significant difference in the descriptive markers age, BMI, BF% and the marker of interest PDFF$_{SC}$ in Mann-Whitney U testing. Double checking this reduces possible confounding due to group selection and ensured that the following observations are primarily driven by different CIT results. Still the expected shift in BAT positive individuals towards lower PDFF values or a flattening of the kurtosis was only observed in histograms of BAT positive individuals with low BF%. To a large extent histograms were driven by BF%, demonstrating once again that body adiposity seems to be the main driver for PDFF measurements.

So far, no attention was given to T_2^* values, although T_2^* relaxation times promise additional information regarding the difference of BAT and WAT. Studies report shorter T_2^* in the supraclavicular fat depot [57, 58, 61, 66, 95], probably due to microstructural inhomogeneity, iron rich mitochondria, higher perfusion, higher oxygenation, and higher water content. However, the reported values are dispersed widely. A corresponding investigation [66] found 6-echo data insufficient for proper T_2^* investigation, with higher accuracy and lower standard deviations for T_2^* values, when data was gathered with an increased number of echoes. Consequently, 6-echo T_2^* values were only considered in comparison to 12-echo data, but not as a diagnostic parameter for BAT. The present comparison of 6- and 12-echo data resulted in a significant difference for both PDFF$_{SC}$ and for PDFF$_{GLU}$, with higher PDFF values in 12-echo data. While differences in PDFF were small but significant, the observed differences in $T_2^*_{SC}$ and $T_2^*_{GLU}$ were major and highly significant. Those results are in line with the above-mentioned publication [66]. Regarding the differentiation of BAT and WAT via supraclavicular and gluteal T_2^* measurements, the evaluated 12-echo data presented significantly different $T_2^*_{SC}$ and $T_2^*_{GLU}$, with shorter supraclavicular relaxation times. These results are consistent

with corresponding literature [57, 58, 61, 66, 95] and support the claim of existing BAT in the supraclavicular region. However, this study investigated MRI parameters under thermoneutrality, but T_2^* measurements, driven by perfusion and oxygenation, highlight functional differences of BAT and WAT. Therefore, T_2^* values are of greater interest, if MRI data is gathered under thermal challenges or other BAT activation.

For the sake of completeness, the correlations of $T_2^*{}_{SC}$ and CIT were evaluated in 12-echo data according to the approach used for PDFF evaluation. In the whole cohort no association was detected, while the normal-weight subgroup and the normal BF% subgroup showed a significant inverse correlation of $T_2^*{}_{SC}$ and CIT, with shorter relaxation times being accompanied by a higher thermogenic potential, accentuating the concept of brown adipocytes existing in the supraclavicular fossa influencing energy expenditure especially under cold exposure [100, 101]. Interestingly, T_2^* values seem to be influenced by body adiposity in a similar manner as PDFF measurements. Most likely body adiposity affects the microscopic homogeneity component of T_2^* measurements, but more detailed explorations are needed.

7.3 Strengths and limitations

A major strength of the present investigation lies in the efforts made concerning data quality, by focusing on meticulous data acquisition and processing from the start: For example the applied breathing trigger for supraclavicular PDFF mapping reduces noise, blurring, and partial volume of the raw data and distinguishes this study from others in the field [99]. Also, the semiautomatic segmentation method with clear and upfront defined segmentation criteria ensured validity and reproducibility, demonstrated in the tested interrater reliability. Moreover, the automatically applied erosion and threshold protocols reduced partial volume effects and were fully reproducible. Regarding CIT measurements, the cooling protocol was designed with care according to Lans et al. [81], ensuring participants were kept above their individual shivering threshold. Additionally, indirect calorimetry measurements were only performed during steady state conditions. When the importance of body adiposity as confounding factor became clear, the diagnostic performance of BMI was questioned and the BIA-based BF% was validated with care via the MRI-based TF%. This ensured correct and robust grouping by adiposity, enabling an adequate evaluation of PDFF$_{SC}$ with minimized confounding. Furthermore, this led to the development of the novel marker PDFF$_{DEL}$, which accounts for confounding body adiposity and allowed assessment of CIT in relation to PDFF regardless of

the individuals nutritional status. The development of $PDFF_{DEL}$, as quick and easy assessed MRI-marker independent from body adiposity, is the major strength of this study.

Regarding study limitations, the most important is the lack of histological validation via biopsy. It is still the gold standard for adipose tissue characterization and without biopsies the presence of BAT cannot be indubitably proven. However, this level of invasiveness was not appropriate and informative value of biopsies with immunohistochemical staining of the UCP1-protein is limited to BAT presence. It would still lack more details regarding the individual's thermogenic potential. Therefore, quantitative MRI measurements in relation to the functional BAT capacity cannot really be validated via histology, in particular since UCP-1 independent thermogenesis seems to play a large role in humans [102, 103]. Other restrictions are derived from the complicated anatomy of the supraclavicular fossa, with high partial volume effects even after the applied erosion and thresholding protocols. Further the isotropic voxel size with 1.5mm in each dimension contributes to partial volume effects, derived from small vessels, lymph nodes, and other smaller anatomical structures. Those effects will always be greater in the supraclavicular ROI, compared to the gluteal ROI, located in a more homogenous tissue. Furthermore, average PDFF values will always include a mixture of BAT and WAT existing next to each other, thus only delivering indications if BAT or WAT constitutes the main share of the investigated volume. High variability in indirect calorimetry and in PDFF measurements, alongside individual adiposity, and tissue morphology lead to a low predictive value of CIT and PDFF, due to error-prone methods. This remains an issue worth noticing, even after all the here taken precautions like steady state correction, applied breathing trigger, and the validation of semiautomatic segmentation. Therefore, the presented data must be interpreted with caution and needs validation in prospective studies with a larger sample size. Simultaneous assessment of CIT and MRI was never intended in the study design, since $PDFF_{SC}$ is used as morphological parameter detached from thermal challenges, but in some participants the two measurements were carried out with a large time interval in between, potentially missing adaptation of supraclavicular composition due to metabolic homeostasis. Finally, the association of energy expenditure and BAT is questioned from time to time, with one study reporting deep muscle tissue contributing to thermogenesis [104], thus it is not conclusively clarified if the measured CIT is substantially derived from BAT activity.

8   Conclusion

Evaluating the association between $PDFF_{SC}$ and CIT was the main goal of the present investigation. Hereby CIT can be seen as functional parameter of BAT, characterizing the individual's capacity for calorie combustion in brown adipocytes, while the MRI parameter $PDFF_{SC}$ serves as morphological parameter of the BAT organ. Detecting existing BAT depots via MRI, promises a quick and easy evaluation of an individual's thermogenic potential. Hopefully, identifying individuals with an existing BAT organ as possible treatment target for obesity and metabolic syndrome. This would need a reliable and easy detection method, also applicable in individuals with overweight or obesity.

The present study found evidence for an existing relation of $PDFF_{SC}$ and CIT. However, this association was only found in lean individuals with normal BF%, showing once again the interdependency of PDFF and adiposity. Apparently, it is inevitable that adiposity drives PDFF measurements to a certain degree, but the newly developed marker $PDFF_{DEL}$ was impacted far less. This study shows that intraindividual referencing to WAT-PDFF, can function as a corrective for adiposity. The $PDFF_{DEL}$ measures the intraindividual difference of gluteal and supraclavicular PDFF and shows a significant association with CIT. These results render $PDFF_{DEL}$ as possible surrogate marker not only for BAT detection, but also quantification of an individual's thermogenic capacity, mostly independent from body adiposity. Due to a rather small sample size and error susceptibility of both CIT and PDFF measurements, larger prospective observational studies are needed to validate the power of $PDFF_{DEL}$ as approximation for CIT. However, if $PDFF_{DEL}$ can be validated it could pave the way for future clinical research and even implement BAT as treatment target for overweight, obesity and metabolic syndrome.

9 <u>List of tables</u>

10 List of Figures

11 <u>List of symbols and abbreviations</u>

A	Cross section
ATP	adenosine triphosphate
B_0	magnetic field
BAT	brown adipose tissue
BF%	body fat percentage
BIA	body impedance analysis
BMR	basal metabolic rate
CIT	Cold-induced thermogenesis
cm	Centimeters
CO_2	carbon dioxide
CT	computer tomography
DEXA	dual energy X-ray absorption
DRKS	German clinical trials register
F	fat signal
FDG	^{18}F-fluorodeoxyglucose
FID	free-induction Decay
H	hydrogen
^{1}H	protons of hydrogen
IP	in-phase
kcal	kilocalories
kg	kilograms
L	length
m	meter
M	net-magnetic moment
min	minutes

ml	milliliter
MRI	magnetic resonance imaging
MRS	magnetic resonance spectroscopy
ms	milliseconds
MSOT	multispectral optoacoustic imaging
N	number
NFT	non-fatty tissue
O_2	oxygen
OP	opposed-phase
p	P-value (p)
PDFF	Proton density fat fraction
$PDFF_{DEL}$	Delta proton density fat fraction
$PDFF_{GLU}$	Gluteal proton density fat fraction
$PDFF_{SC}$	Supraclavicular proton density fat fraction
PET	positron-emission tomography
QIMS	Quantitative Imaging in Medicine and Surgery
R	resistance
R2*	reciprocal value of T_2^*
REE	resting energy expenditure
RF	radio frequency pulse
rho	Spearman's rho
ROI	region of interest
SAT	subcutaneous adipose tissue
SD	standard deviation
SFF	signal fat fraction
T_1	longitudinal relaxation time
T_2	transversal relaxation time

T_2^*	T_2-star / in-vivo observed transversal relaxation time
$T_2^*_{GLU}$	Gluteal T_2^*
$T_2^*_{SC}$	Supraclavicular T_2^*
TE	echo time
TF%	trunk fat percentage
TR	repetition time
TUM	Technical University Munich
UCP1	uncoupling protein 1
V	volume
VAT	visceral adipose tissue
VCO2	volume of produced carbon dioxide
VO_2	volume of consumed oxygen
VOL_{SC}	Volume of the supraclavicular fossa
W	water signal
WAT	white adipose tissue
WHO	world health organization
γ	gyromagnetic ratio
ρ	specific resistivity
ω	Larmor frequency

12 <u>References</u>

[1]   Kershaw EE, Flier JS. Adipose tissue as an endocrine organ. The Journal of Clinical Endocrinology & Metabolism. 2004;89(6):2548-56.

[2]   Grundy SM, Brewer Jr HB, Cleeman JI, Smith Jr SC, Lenfant C. Definition of metabolic syndrome: report of the National Heart, Lung, and Blood Institute/American Heart Association conference on scientific issues related to definition. Circulation. 2004;109(3):433-8.

[3]   Callow AD. Cardiovascular disease 2005—the global picture. Vascular pharmacology. 2006;45(5):302-7.

[4]   Balakumar P, Maung-U K, Jagadeesh G. Prevalence and prevention of cardiovascular disease and diabetes mellitus. Pharmacological research. 2016;113:600-9.

[5]   Organization WH. World health statistics 2020. 2020.

[6]   Kopelman PG. Obesity as a medical problem. Nature. 2000;404(6778):635-43.

[7]   Himms-Hagen J. Does Thermoregulatory Feeding Occur in Newborn Infants? A Novel View of the Role of Brown Adipose Tissue Thermo genesis in Control of Food Intake. Obesity Research. 1995;3(4):361-9.

[8]   Enerback S. Human brown adipose tissue. Cell Metab. 2010;11(4):248-52.

[9]   Bartelt A, Bruns OT, Reimer R, Hohenberg H, Ittrich H, Peldschus K, Kaul MG, Tromsdorf UI, Weller H, Waurisch C, Eychmuller A, Gordts PL, Rinninger F, Bruegelmann K, Freund B, Nielsen P, Merkel M, Heeren J. Brown adipose tissue activity controls triglyceride clearance. Nat Med. 2011;17(2):200-5.

[10]   Fedorenko A, Lishko PV, Kirichok Y. Mechanism of fatty-acid-dependent UCP1 uncoupling in brown fat mitochondria. Cell. 2012;151(2):400-13.

[11]   Blondin DP, Labbe SM, Tingelstad HC, Noll C, Kunach M, Phoenix S, Guerin B, Turcotte EE, Carpentier AC, Richard D, Haman F. Increased brown adipose tissue oxidative capacity in cold-acclimated humans. J Clin Endocrinol Metab. 2014;99(3):E438-46.

[12]   Muzik O, Mangner TJ, Granneman JG. Assessment of oxidative metabolism in brown fat using PET imaging. Front Endocrinol (Lausanne). 2012;3:15.

[13]   Yoneshiro T, Aita S, Matsushita M, Kameya T, Nakada K, Kawai Y, Saito M. Brown adipose tissue, whole-body energy expenditure, and thermogenesis in healthy adult men. Obesity (Silver Spring). 2011;19(1):13-6.

[14]   Brychta RJ, Chen KY. Cold-induced thermogenesis in humans. Eur J Clin Nutr. 2017;71(3):345-52.

[15]   Cypess AM, Lehman S, Williams G, Tal I, Rodman D, Goldfine AB, Kuo FC, Palmer EL, Tseng YH, Doria A, Kolodny GM, Kahn CR. Identification and importance of brown adipose tissue in adult humans. N Engl J Med. 2009;360(15):1509-17.

[16]   van Marken Lichtenbelt WD, Vanhommerig JW, Smulders NM, Drossaerts JM, Kemerink GJ, Bouvy ND, Schrauwen P, Teule GJ. Cold-activated brown adipose tissue in healthy men. N Engl J Med. 2009;360(15):1500-8.

[17]   Virtanen KA, Lidell ME, Orava J, Heglind M, Westergren R, Niemi T, Taittonen M, Laine J, Savisto NJ, Enerback S, Nuutila P. Functional brown adipose tissue in healthy adults. N Engl J Med. 2009;360(15):1518-25.

[18]   Wu M, Junker D, Branca RT, Karampinos DC. Magnetic Resonance Imaging Techniques for Brown Adipose Tissue Detection. Front Endocrinol (Lausanne). 2020;11:421.

[19]   Hu HH. Magnetic Resonance of Brown Adipose Tissue: A Review of Current Techniques. Crit Rev Biomed Eng. 2015;43(2-3):161-81.

[20]   Karampinos DC, Weidlich D, Wu M, Hu HH, Franz D. Techniques and Applications of Magnetic Resonance Imaging for Studying Brown Adipose Tissue Morphometry and Function. Handb Exp Pharmacol. 2019;251:299-324.

[21]   Dixon WT. Simple proton spectroscopic imaging. Radiology. 1984;153(1):189-94.

[22]   Chooi YC, Ding C, Magkos F. The epidemiology of obesity. Metabolism. 2019;92:6-10.

[23]   World Health O. Obesity : Preventing and managing the global epidemic. Geneva: World Health Organization; 2000.

[24]   Cypess AM, Kahn CR. The role and importance of brown adipose tissue in energy homeostasis. Current opinion in pediatrics. 2010;22(4):478.

[25]   Maliszewska K, Kretowski A. Brown adipose tissue and its role in insulin and glucose homeostasis. International journal of molecular sciences. 2021;22(4):1530.

[26]   Stanford KI, Middelbeek RJ, Townsend KL, An D, Nygaard EB, Hitchcox KM, Markan KR, Nakano K, Hirshman MF, Tseng Y-H. Brown adipose tissue regulates glucose homeostasis and insulin sensitivity. The Journal of clinical investigation. 2012;123(1).

[27]   Cinti S. The adipose organ: morphological perspectives of adipose tissues. Proceedings of the Nutrition Society. 2001;60(3):319-28.

[28]   Cinti S. The adipose organ at a glance. Disease models & mechanisms. 2012;5(5):588-94.

[29]   Lidell ME, Betz MJ, Dahlqvist Leinhard O, Heglind M, Elander L, Slawik M, Mussack T, Nilsson D, Romu T, Nuutila P, Virtanen KA, Beuschlein F, Persson A, Borga M, Enerback S. Evidence for two types of brown adipose tissue in humans. Nat Med. 2013;19(5):631-4.

[30]   Seale P, Bjork B, Yang W, Kajimura S, Chin S, Kuang S, Scimè A, Devarakonda S, Conroe HM, Erdjument-Bromage H, Tempst P, Rudnicki MA, Beier DR, Spiegelman BM. PRDM16 controls a brown fat/skeletal muscle switch. Nature. 2008;454(7207):961-7.

[31]   Betz MJ, Enerbäck S. Human brown adipose tissue: what we have learned so far. Diabetes. 2015;64(7):2352-60.

[32]   Heaton JM. The distribution of brown adipose tissue in the human. Journal of anatomy. 1972;112(Pt 1):35.

[33]   Nedergaard J, Bengtsson T, Cannon B. Unexpected evidence for active brown adipose tissue in adult humans. American Journal of Physiology-Endocrinology and Metabolism. 2007.

[34] Sacks H, Symonds ME. Anatomical locations of human brown adipose tissue: functional relevance and implications in obesity and type 2 diabetes. Diabetes. 2013;62(6):1783-90.

[35] Frontini A, Cinti S. Distribution and development of brown adipocytes in the murine and human adipose organ. Cell metabolism. 2010;11(4):253-6.

[36] Porter C, Herndon DN, Chondronikola M, Chao T, Annamalai P, Bhattarai N, Saraf MK, Capek KD, Reidy PT, Daquinag AC. Human and mouse brown adipose tissue mitochondria have comparable UCP1 function. Cell metabolism. 2016;24(2):246-55.

[37] Cypess AM, White AP, Vernochet C, Schulz TJ, Xue R, Sass CA, Huang TL, Roberts-Toler C, Weiner LS, Sze C. Anatomical localization, gene expression profiling and functional characterization of adult human neck brown fat. Nature medicine. 2013;19(5):635-9.

[38] Liu X, Cervantes C, Liu F. Common and distinct regulation of human and mouse brown and beige adipose tissues: a promising therapeutic target for obesity. Protein & Cell. 2017;8(6):446-54.

[39] Jespersen NZ, Larsen TJ, Peijs L, Daugaard S, Homoe P, Loft A, de Jong J, Mathur N, Cannon B, Nedergaard J, Pedersen BK, Moller K, Scheele C. A classical brown adipose tissue mRNA signature partly overlaps with brite in the supraclavicular region of adult humans. Cell Metab. 2013;17(5):798-805.

[40] Sidossis L, Kajimura S. Brown and beige fat in humans: thermogenic adipocytes that control energy and glucose homeostasis. The Journal of clinical investigation. 2015;125(2):478-86.

[41] Hany TF, Gharehpapagh E, Kamel EM, Buck A, Himms-Hagen J, von Schulthess GK. Brown adipose tissue: a factor to consider in symmetrical tracer uptake in the neck and upper chest region. Eur J Nucl Med Mol Imaging. 2002;29(10):1393-8.

[42] Saito M, Okamatsu-Ogura Y, Matsushita M, Watanabe K, Yoneshiro T, Nio-Kobayashi J, Iwanaga T, Miyagawa M, Kameya T, Nakada K, Kawai Y, Tsujisaki M. High incidence of metabolically active brown adipose tissue in healthy adult humans: effects of cold exposure and adiposity. Diabetes. 2009;58(7):1526-31.

[43]   Saito M, Matsushita M, Yoneshiro T, Okamatsu-Ogura Y. Brown adipose tissue, diet-induced thermogenesis, and thermogenic food ingredients: from mice to men. Frontiers in endocrinology. 2020;11:222.

[44]   Cannon B, Nedergaard J. Brown adipose tissue: function and physiological significance. Physiological reviews. 2004.

[45]   Marlatt KL, Ravussin E. Brown Adipose Tissue: an Update on Recent Findings. Curr Obes Rep. 2017;6(4):389-96.

[46]   Blondin DP, Labbe SM, Noll C, Kunach M, Phoenix S, Guerin B, Turcotte EE, Haman F, Richard D, Carpentier AC. Selective Impairment of Glucose but Not Fatty Acid or Oxidative Metabolism in Brown Adipose Tissue of Subjects With Type 2 Diabetes. Diabetes. 2015;64(7):2388-97.

[47]   Orava J, Nuutila P, Lidell Martin E, Oikonen V, Noponen T, Viljanen T, Scheinin M, Taittonen M, Niemi T, Enerbäck S, Virtanen Kirsi A. Different Metabolic Responses of Human Brown Adipose Tissue to Activation by Cold and Insulin. Cell Metabolism. 2011;14(2):272-9.

[48]   Yoneshiro T, Saito M. Activation and recruitment of brown adipose tissue as anti-obesity regimens in humans. Ann Med. 2015;47(2):133-41.

[49]   Gupta RD, Ramachandran R, Venkatesan P, Anoop S, Joseph M, Thomas N. Indirect Calorimetry: From Bench to Bedside. Indian J Endocrinol Metab. 2017;21(4):594-9.

[50]   Weir JB. New methods for calculating metabolic rate with special reference to protein metabolism. J Physiol. 1949;109(1-2):1-9.

[51]   Levitt MH. Spin dynamics: basics of nuclear magnetic resonance: John Wiley & Sons; 2013.

[52]   Tofts P. Quantitative MRI of the brain: measuring changes caused by disease: John Wiley & Sons; 2005.

[53]   Cambridge Dictionary [Available from: https://dictionary.cambridge.org/de/worterbuch/englisch/quantify.

[54]   Reeder SB, Cruite I, Hamilton G, Sirlin CB. Quantitative Assessment of Liver Fat with Magnetic Resonance Imaging and Spectroscopy. Journal of magnetic resonance imaging : JMRI. 2011;34(4):729-49.

[55]   Reeder SB, Hu HH, Sirlin CB. Proton density fat-fraction: A standardized mr-based biomarker of tissue fat concentration. Journal of Magnetic Resonance Imaging. 2012;36(5):1011-4.

[56]   Franssens BT, Eikendal AL, Leiner T, van der Graaf Y, Visseren FL, Hoogduin JM. Reliability and agreement of adipose tissue fat fraction measurements with water-fat MRI in patients with manifest cardiovascular disease. NMR Biomed. 2016;29(1):48-56.

[57]   Gifford A, Towse TF, Walker RC, Avison MJ, Welch EB. Characterizing active and inactive brown adipose tissue in adult humans using PET-CT and MR imaging. Am J Physiol Endocrinol Metab. 2016;311(1):E95-E104.

[58]   Holstila M, Pesola M, Saari T, Koskensalo K, Raiko J, Borra RJ, Nuutila P, Parkkola R, Virtanen KA. MR signal-fat-fraction analysis and T2* weighted imaging measure BAT reliably on humans without cold exposure. Metabolism. 2017;70:23-30.

[59]   Koskensalo K, Raiko J, Saari T, Saunavaara V, Eskola O, Nuutila P, Saunavaara J, Parkkola R, Virtanen KA. Human Brown Adipose Tissue Temperature and Fat Fraction Are Related to Its Metabolic Activity. The Journal of Clinical Endocrinology & Metabolism. 2017;102(4):1200-7.

[60]   Lundstrom E, Strand R, Johansson L, Bergsten P, Ahlstrom H, Kullberg J. Magnetic resonance imaging cooling-reheating protocol indicates decreased fat fraction via lipid consumption in suspected brown adipose tissue. PLoS One. 2015;10(4):e0126705.

[61]   McCallister A, Zhang L, Burant A, Katz L, Branca RT. A pilot study on the correlation between fat fraction values and glucose uptake values in supraclavicular fat by simultaneous PET/MRI. Magn Reson Med. 2017;78(5):1922-32.

[62]   Franz D, Karampinos DC, Rummeny EJ, Souvatzoglou M, Beer AJ, Nekolla SG, Schwaiger M, Eiber M. Discrimination Between Brown and White Adipose Tissue Using a 2-Point Dixon Water-Fat Separation Method in Simultaneous PET/MRI. J Nucl Med. 2015;56(11):1742-7.

[63]   Stahl V, Maier F, Freitag MT, Floca RO, Berger MC, Umathum R, Berriel Diaz M, Herzig S, Weber MA, Dimitrakopoulou-Strauss A, Rink K, Bachert P, Ladd ME, Nagel AM. In vivo assessment of cold stimulation effects on the fat fraction of brown adipose tissue using DIXON MRI. J Magn Reson Imaging. 2017;45(2):369-80.

[64]   Franz D, Weidlich D, Freitag F, Holzapfel C, Drabsch T, Baum T, Eggers H, Witte A, Rummeny EJ, Hauner H, Karampinos DC. Association of proton density fat fraction in adipose tissue with imaging-based and anthropometric obesity markers in adults. Int J Obes (Lond). 2018;42(2):175-82.

[65]   Deng J, Neff LM, Rubert NC, Zhang B, Shore RM, Samet JD, Nelson PC, Landsberg L. MRI characterization of brown adipose tissue under thermal challenges in normal weight, overweight, and obese young men. J Magn Reson Imaging. 2018;47(4):936-47.

[66]   Franz D, Diefenbach MN, Treibel F, Weidlich D, Syvari J, Ruschke S, Wu M, Holzapfel C, Drabsch T, Baum T, Eggers H, Rummeny EJ, Hauner H, Karampinos DC. huh. J Magn Reson Imaging. 2019;50(2):424-34.

[67]   Engin A. The Definition and Prevalence of Obesity and Metabolic Syndrome. In: Engin AB, Engin A, editors. Obesity and Lipotoxicity. Cham: Springer International Publishing; 2017. p. 1-17.

[68]   Okorodudu DO, Jumean MF, Montori VM, Romero-Corral A, Somers VK, Erwin PJ, Lopez-Jimenez F. Diagnostic performance of body mass index to identify obesity as defined by body adiposity: a systematic review and meta-analysis. Int J Obes (Lond). 2010;34(5):791-9.

[69]   Romero-Corral A, Somers VK, Sierra-Johnson J, Thomas RJ, Collazo-Clavell ML, Korinek J, Allison TG, Batsis JA, Sert-Kuniyoshi FH, Lopez-Jimenez F. Accuracy of body mass index in diagnosing obesity in the adult general population. International journal of obesity (2005). 2008;32(6):959-66.

[70]   Kushner RF. Bioelectrical Impedance Analysis: A Review of Principles and Applications. Journal of the American College of Nutrition. 1992;11(2):199-209.

[71]   Bosy-Westphal A, Later W, Hitze B, Sato T, Kossel E, Gluer CC, Heller M, Muller MJ. Accuracy of bioelectrical impedance consumer devices for measurement of body

composition in comparison to whole body magnetic resonance imaging and dual X-ray absorptiometry. Obes Facts. 2008;1(6):319-24.

[72]   Dehghan M, Merchant AT. Is bioelectrical impedance accurate for use in large epidemiological studies? Nutr J. 2008;7:26.

[73]   Demerath EW, Reed D, Rogers N, Sun SS, Lee M, Choh AC, Couch W, Czerwinski SA, Chumlea WC, Siervogel RM, Towne B. Visceral adiposity and its anatomical distribution as predictors of the metabolic syndrome and cardiometabolic risk factor levels. The American Journal of Clinical Nutrition. 2008;88(5):1263-71.

[74]   Liu J, Fox CS, Hickson DA, May WD, Hairston KG, Carr JJ, Taylor HA. Impact of Abdominal Visceral and Subcutaneous Adipose Tissue on Cardiometabolic Risk Factors: The Jackson Heart Study. The Journal of Clinical Endocrinology & Metabolism. 2010;95(12):5419-26.

[75]   Hsu C-H, Lin J-D, Hsieh C-H, Lau SC, Chiang W-Y, Chen Y-L, Pei D, Chang J-B. Adiposity measurements in association with metabolic syndrome in older men have different clinical implications. Nutrition Research. 2014;34(3):219-25.

[76]   Borga M, West J, Bell JD, Harvey NC, Romu T, Heymsfield SB, Dahlqvist Leinhard O. Advanced body composition assessment: from body mass index to body composition profiling. J Investig Med. 2018;66(5):1-9.

[77]   Ross R, Goodpaster B, Kelley D, Boada F. Magnetic resonance imaging in human body composition research: from quantitative to qualitative tissue measurement. Annals of the New York Academy of Sciences. 2000;904(1):12-7.

[78]   Fullmer S, Benson-Davies S, Earthman CP, Frankenfield DC, Gradwell E, Lee PS, Piemonte T, Trabulsi J. Evidence analysis library review of best practices for performing indirect calorimetry in healthy and non–critically ill individuals. Journal of the Academy of Nutrition and Dietetics. 2015;115(9):1417-46. e2.

[79]   Weir JdV. New methods for calculating metabolic rate with special reference to protein metabolism. The Journal of physiology. 1949;109(1-2):1-9.

[80] Mengel LA, Seidl H, Brandl B, Skurk T, Holzapfel C, Stecher L, Claussnitzer M, Hauner H. Gender Differences in the Response to Short-term Cold Exposure in Young Adults. J Clin Endocrinol Metab. 2020;105(5).

[81] van der Lans AA, Hoeks J, Brans B, Vijgen GH, Visser MG, Vosselman MJ, Hansen J, Jorgensen JA, Wu J, Mottaghy FM, Schrauwen P, van Marken Lichtenbelt WD. Cold acclimation recruits human brown fat and increases nonshivering thermogenesis. J Clin Invest. 2013;123(8):3395-403.

[82] Karampinos DC, Yu H, Shimakawa A, Link TM, Majumdar S. T(1)-corrected fat quantification using chemical shift-based water/fat separation: application to skeletal muscle. Magn Reson Med. 2011;66(5):1312-26.

[83] Liu CY, McKenzie CA, Yu H, Brittain JH, Reeder SB. Fat quantification with IDEAL gradient echo imaging: correction of bias from T(1) and noise. Magn Reson Med. 2007;58(2):354-64.

[84] Eggers H, Brendel B, Duijndam A, Herigault G. Dual-echo Dixon imaging with flexible choice of echo times. Magn Reson Med. 2011;65(1):96-107.

[85] Yushkevich PA, Piven J, Hazlett HC, Smith RG, Ho S, Gee JC, Gerig G. User-guided 3D active contour segmentation of anatomical structures: significantly improved efficiency and reliability. Neuroimage. 2006;31(3):1116-28.

[86] Cordes C, Dieckmeyer M, Ott B, Shen J, Ruschke S, Settles M, Eichhorn C, Bauer JS, Kooijman H, Rummeny EJ, Skurk T, Baum T, Hauner H, Karampinos DC. MR-detected changes in liver fat, abdominal fat, and vertebral bone marrow fat after a four-week calorie restriction in obese women. J Magn Reson Imaging. 2015;42(5):1272-80.

[87] Obesity: preventing and managing the global epidemic. Report of a WHO consultation. World Health Organ Tech Rep Ser. 2000;894:i-xii, 1-253.

[88] Snitker S. Use of body fatness cutoff points. Mayo Clin Proc. 2010;85(11):1057; author reply -8.

[89] Frankenfield DC, Rowe WA, Cooney RN, Smith JS, Becker D. Limits of body mass index to detect obesity and predict body composition. Nutrition. 2001;17(1):26-30.

[90] De Lorenzo A, Soldati L, Sarlo F, Calvani M, Di Lorenzo N, Di Renzo L. New obesity classification criteria as a tool for bariatric surgery indication. World J Gastroenterol. 2016;22(2):681-703.

[91] Ong Frank J, Ahmed Basma A, Oreskovich Stephan M, Blondin Denis P, Haq T, Konyer Norman B, Noseworthy Michael D, Haman F, Carpentier Andre C, Morrison Katherine M, Steinberg Gregory R. Recent advances in the detection of brown adipose tissue in adult humans: a review. Clinical Science. 2018;132(10):1039-54.

[92] Deng J, Schoeneman SE, Zhang H, Kwon S, Rigsby CK, Shore RM, Josefson JL. MRI characterization of brown adipose tissue in obese and normal-weight children. Pediatric Radiology. 2015;45(11):1682-9.

[93] Franssens BT, Hoogduin H, Leiner T, van der Graaf Y, Visseren FLJ. Relation between brown adipose tissue and measures of obesity and metabolic dysfunction in patients with cardiovascular disease. J Magn Reson Imaging. 2017;46(2):497-504.

[94] Hu HH, Perkins TG, Chia JM, Gilsanz V. Characterization of human brown adipose tissue by chemical-shift water-fat MRI. American Journal of Roentgenology. 2013;200(1):177-83.

[95] Hu HH, Yin L, Aggabao PC, Perkins TG, Chia JM, Gilsanz V. Comparison of brown and white adipose tissues in infants and children with chemical-shift-encoded water-fat MRI. J Magn Reson Imaging. 2013;38(4):885-96.

[96] Karcher HS, Holzwarth R, Mueller HP, Ludolph AC, Huber R, Kassubek J, Pinkhardt EH. Body fat distribution as a risk factor for cerebrovascular disease: an MRI-based body fat quantification study. Cerebrovasc Dis. 2013;35(4):341-8.

[97] Rasmussen JM, Entringer S, Nguyen A, van Erp TG, Burns J, Guijarro A, Oveisi F, Swanson JM, Piomelli D, Wadhwa PD, Buss C, Potkin SG. Brown adipose tissue quantification in human neonates using water-fat separated MRI. PLoS One. 2013;8(10):e77907.

[98] Sun L, Verma S, Michael N, Chan SP, Yan J, Sadananthan SA, Camps SG, Goh HJ, Govindharajulu P, Totman J, Townsend D, Goh JP-N, Sun L, Boehm BO, Lim SC, Sze SK, Henry CJ, Hu HH, Velan SS, Leow MK-S. Brown Adipose Tissue: Multimodality

Evaluation by PET, MRI, Infrared Thermography, and Whole-Body Calorimetry (TACTICAL-II). Obesity. 2019;27(9):1434-42.

[99]   Gashi G, Madoerin P, Maushart CI, Michel R, Senn JR, Bieri O, Betz MJ. MRI characteristics of supraclavicular brown adipose tissue in relation to cold-induced thermogenesis in healthy human adults. J Magn Reson Imaging. 2019;50(4):1160-8.

[100]   Cannon B, Nedergaard J. Brown adipose tissue: function and physiological significance. Physiol Rev. 2004;84(1):277-359.

[101]   Rothwell NJ, Stock MJ. Luxuskonsumption, diet-induced thermogenesis and brown fat: the case in favour. Clin Sci (Lond). 1983;64(1):19-23.

[102]   Ikeda K, Yamada T. UCP1 Dependent and Independent Thermogenesis in Brown and Beige Adipocytes. Front Endocrinol (Lausanne). 2020;11:498.

[103]   Roesler A, Kazak L. UCP1-independent thermogenesis. Biochemical Journal. 2020;477(3):709-25.

[104]   M UD, Raiko J, Saari T, Kudomi N, Tolvanen T, Oikonen V, Teuho J, Sipila HT, Savisto N, Parkkola R, Nuutila P, Virtanen KA. Human brown adipose tissue [(15)O]O2 PET imaging in the presence and absence of cold stimulus. Eur J Nucl Med Mol Imaging. 2016;43(10):1878-86.